

# O(<sup>3</sup>P) + CO<sub>2</sub> Collisions at Hyperthermal Energies: Dynamics of Nonreactive Scattering, Oxygen Isotope Exchange, and Oxygen-Atom Abstraction

Laurence Y. Yeung<sup>†</sup> and Mitchio Okumura<sup>\*</sup>

Division of Chemistry and Chemical Engineering, California Institute of Technology, Pasadena, California 91125, United States

Jianming Zhang and Timothy K. Minton<sup>\*</sup>

Department of Chemistry and Biochemistry, Montana State University, Bozeman, Montana 59717, United States

Jeffrey T. Paci

Department of Chemistry, University of Victoria, Victoria, British Columbia V8W 3V6, Canada, and Department of Chemistry, Northwestern University, Evanston, Illinois 60208, United States

Amir Karton and Jan M. L. Martin

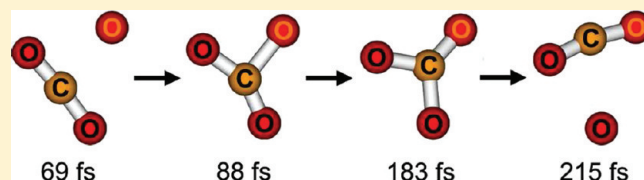
Department of Organic Chemistry, Weizmann Institute of Science, Rehovot, IL-76100, Israel

Jon P. Camden<sup>†</sup> and George C. Schatz<sup>\*</sup>

Department of Chemistry, Northwestern University, Evanston, Illinois 60208, United States

 Supporting Information

**ABSTRACT:** The dynamics of O(<sup>3</sup>P) + CO<sub>2</sub> collisions at hyperthermal energies were investigated experimentally and theoretically. Crossed-molecular-beams experiments at  $\langle E_{\text{coll}} \rangle = 98.8 \text{ kcal mol}^{-1}$  were performed with isotopically labeled <sup>12</sup>C<sup>18</sup>O<sub>2</sub> to distinguish products of nonreactive scattering from those of reactive scattering. The following product channels were observed: elastic and inelastic scattering (<sup>16</sup>O(<sup>3</sup>P) + <sup>12</sup>C<sup>18</sup>O<sub>2</sub>), isotope exchange (<sup>18</sup>O + <sup>16</sup>O<sup>12</sup>C<sup>18</sup>O), and oxygen-atom abstraction (<sup>18</sup>O<sup>16</sup>O + <sup>12</sup>C<sup>18</sup>O). Stationary points on the two lowest triplet potential energy surfaces of the O(<sup>3</sup>P) + CO<sub>2</sub> system were characterized at the CCSD(T)/aug-cc-pVTZ level of theory and by means of W4 theory, which represents an approximation to the relativistic basis set limit, full-configuration-interaction (FCI) energy. The calculations predict a planar CO<sub>3</sub>(C<sub>2v</sub>, <sup>3</sup>A'') intermediate that lies 16.3 kcal mol<sup>-1</sup> (W4 FCI excluding zero point energy) above reactants and is approached by a C<sub>2v</sub> transition state with energy 24.08 kcal mol<sup>-1</sup>. Quasi-classical trajectory (QCT) calculations with collision energies in the range 23–150 kcal mol<sup>-1</sup> were performed at the B3LYP/6-311G(d) and BMK/6-311G(d) levels. Both reactive channels observed in the experiment were predicted by these calculations. In the isotope exchange reaction, the experimental center-of-mass (c.m.) angular distribution,  $T(\theta_{\text{c.m.}})$ , of the <sup>16</sup>O<sup>12</sup>C<sup>18</sup>O products peaked along the initial CO<sub>2</sub> direction (backward relative to the direction of the reagent O atoms), with a smaller isotropic component. The product translational energy distribution,  $P(E_{\text{T}})$ , had a relatively low average of  $\langle E_{\text{T}} \rangle = 35 \text{ kcal mol}^{-1}$ , indicating that the <sup>16</sup>O<sup>12</sup>C<sup>18</sup>O products were formed with substantial internal energy. The QCT calculations give c.m.  $P(E_{\text{T}})$  and  $T(\theta_{\text{c.m.}})$  distributions and a relative product yield that agree qualitatively with the experimental results, and the trajectories indicate that exchange occurs through a short-lived CO<sub>3</sub>\* intermediate. A low yield for the abstraction reaction was seen in both the experiment and the theory. Experimentally, a fast and weak <sup>16</sup>O<sup>18</sup>O product signal from an abstraction reaction was observed, which could only be detected in the forward direction. A small number of QCT trajectories leading to abstraction were observed to occur primarily via a transient CO<sub>3</sub> intermediate, albeit only at high collision energies (149 kcal mol<sup>-1</sup>). The oxygen isotope exchange mechanism for CO<sub>2</sub> in collisions with ground state O atoms is a newly discovered pathway through which oxygen isotopes may be cycled in the upper atmosphere, where O(<sup>3</sup>P) atoms with hyperthermal translational energies can be generated by photodissociation of O<sub>3</sub> and O<sub>2</sub>.

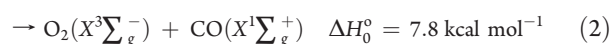
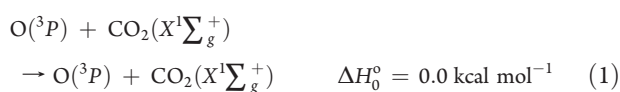


**Received:** August 20, 2011  
**Revised:** October 19, 2011  
**Published:** December 20, 2011

## I. INTRODUCTION

Atomic-oxygen radicals in the atmosphere play an important role in regulating the oxidative and radiative balance of Earth. Photodissociation of molecular oxygen ( $O_2$ ) and ozone ( $O_3$ ) by solar ultraviolet radiation produces not only electronically excited  $O(^1D)$  and  $O(^1S)$ , but also ground-state  $O(^3P)$ , with velocities as high as  $6 \text{ km s}^{-1}$ .<sup>1,2</sup>  $O(^3P)$  has received less attention than  $O(^1D)$  and  $O(^1S)$ , however, because it is less reactive at low collision energies. Yet its important roles in the terrestrial mesosphere and thermosphere are widely recognized. For instance, its collisions with  $CO_2$  significantly influence the population of  $CO_2(010)$ , whose emission at  $15 \mu\text{m}$  cools the atmosphere and regulates the height of the mesopause.<sup>3</sup> In addition,  $O(^3P)$  might collide with  $CO_2$  in space vehicle exhaust streams at relative velocities near  $8 \text{ km s}^{-1}$ , resulting in  $O(^3P)-CO_2$  collisions with energies near  $100 \text{ kcal mol}^{-1}$ .

These high collision energies exceed barriers to (1)  $CO_3$  formation, leading to oxygen-atom exchange and (2) oxygen-atom abstraction on the triplet potential energy surface (PES).<sup>4–7</sup> The enthalpies associated with these reactions are



An isotope exchange reaction analogous to reaction 1, between metastable excited  $O(^1D)$  and ground state  $CO_2$  in the stratosphere,<sup>6,8–16</sup> alters the stable isotope composition of  $CO_2$ , allowing this composition to be used as a tracer of  $O(^1D)$  atoms<sup>17</sup> and atmospheric transport.<sup>18</sup> The stable isotope composition of  $CO_2$  has also been proposed as a tracer of biogeochemical cycles on annual and decadal time scales.<sup>16,19</sup> Reactions 1 and 2 may further alter the isotopic composition of upper atmospheric  $CO_2$ .

Early studies of the  $O(^3P) + CO_2$  system were primarily theoretical and focused on vibrational-state-specific energy transfer.<sup>20–23</sup> The energy-transfer mechanism was found to be primarily impulsive at high collision energies, like that of collisions between  $CO_2$  and noble gases.<sup>22–24</sup> More recent quantum-chemistry calculations on the  $O(^3P) + CO_2(010)$  system indicate that vibrational-to-translational energy transfer is sensitive to the total angular momentum  $J$  at thermal collision energies and that the importance of spin–orbit coupling decreases with increasing collision energy.<sup>25,26</sup> State-specific excitation and relaxation in  $O(^3P) + CO_2$  collisions have since been studied experimentally. Studies of  $CO_2(001)$  excitation by hyperthermal  $O(^3P)$  provided evidence that reaction (2), which is important in combustion chemistry,<sup>27</sup> yields vibrationally excited CO products.<sup>28,29</sup> State-specific relaxation of  $CO_2(010)$  by way of collision with  $O(^3P)$  has also been examined.<sup>30,31</sup> However, no mechanisms were proposed, and the effects of an isotope exchange pathway on the inelastic scattering dynamics have not been investigated.

Here, we present the results of theoretical and crossed-molecular-beams studies of  $^{16}O(^3P) + C^{18}O_2$  collisions at hyperthermal collision energies. Direct dynamics calculations using the quasi-classical trajectory (QCT) method on the lowest-energy triplet PES are compared with the results from the experiment with an average collision energy of  $\langle E_{\text{coll}} \rangle = 98.8 \text{ kcal mol}^{-1}$ . This experiment–theory comparison was augmented by high-level

electronic structure calculations to determine energies of selected stationary points on the lowest two triplet potential energy surfaces, with efforts primarily focused on the lowest state. Reactions 1 and 2 were observed both theoretically and experimentally. Center-of-mass (c.m.) angular and translational energy distributions for the nonreactive scattering and for the oxygen isotope exchange reaction were obtained. The implications for atomic oxygen cycling through  $CO_2$  in the atmosphere are discussed.

## II. THEORETICAL METHODS

**A. Electronic Structure Calculations.** Stationary points on the lowest triplet PES of  $CO_3$ , which has  $^3A''$  electronic symmetry, were characterized at the B3LYP/6-311G(d),<sup>32–34</sup> BMK/6-311G(d),<sup>35</sup> and CCSD(T)/aug-cc-pVTZ<sup>36,37</sup> levels of theory using Q-Chem<sup>38</sup> and MOLPRO.<sup>39</sup> Transition states were confirmed by inspection of their associated vibrational frequencies. B3LYP/6-311G(d) calculations indicated that collision energies in excess of  $250 \text{ kcal mol}^{-1}$  are required to open reactive channels other than 1 and 2, so these other channels were not considered further.

The  $O(^3P) + CO_2$  surface is triply degenerate at large  $O(^3P)-CO_2$  separations, giving rise to two  $^3A''$  and one  $^3A'$  electronic states. Properties of the stationary points on the lowest-energy state, which has  $^3A''$  electronic symmetry, are summarized in Figures 1 and 2 and Table 1. The  $^3A'$  electronic state is very close in energy to the lowest  $^3A''$  electronic state in the regions of the PES surrounding  $CO_3$  and its associated transition state, so the characteristics of these structures on the  $^3A'$  electronic state are also presented. All structures are planar and all have  $C_s$  symmetry, except for both  $CO_3$  structures and TS1 ( $^3A'$ ), which have a  $C_{2v}$  symmetry. The TS1 transition states and  $CO_3$  bound states are associated with the  $O(^3P) + CO_2$  isotope exchange reaction. For the oxygen-atom abstraction reaction, the most important transition states are TS2 and TS3, although we found and characterized two additional bound states (BS1 and BS2) and two associated transition states (TS4 and TS5), shown in Figure 2b.

W4 calculations were also performed for the stationary points in Figure 1. W4 theory<sup>40</sup> represents a layered extrapolation to the relativistic FCI basis set limit. In particular, it has been shown that the inclusion of successively higher cluster expansion terms results in increasingly fast convergence with increases in basis set size, as these terms increasingly reflect nondynamical rather than dynamical correlation.<sup>40,42</sup> Indeed, the fact that W4 and related methods can be carried out at a realistic computational cost hinges on this behavior. For a set of highly accurate experimental atomization energies (from the Active Thermochemical Tables [ATcT] paradigm of Ruscic et al.),<sup>41</sup> W4 theory obtains a root-mean-square deviation of  $0.08 \text{ kcal mol}^{-1}$ , implying a 95% confidence interval of  $0.16 \text{ kcal mol}^{-1}$ . Of particular relevance to the present study, it should be noted that W4 theory has been found to be remarkably resilient toward multireference character, for example, for strongly multireference systems such as  $O_3$ ,  $F_2O_2$ ,  $F_2O$ ,  $C_2$ , and  $FO$ , W4 predicts atomization energies within  $0.28 \text{ kcal mol}^{-1}$  of the ATcT values (for a more detailed recent assessment of the performance of W4 theory, see ref 43). Table S1 of the Supporting Information (SI) provides the percentage of the nonrelativistic, clamped-nuclei total atomization energy at the bottom of the well (%TAEe) accounted for by the SCF, (T) triples, post-CCSD(T), and  $T_4 + T_5$  contributions.

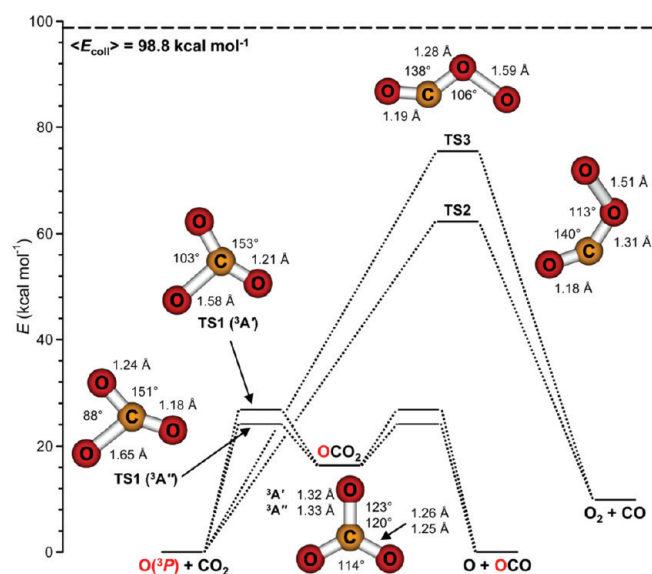


**Figure 1.** Stationary-point structures most relevant to  $\text{O}(^3P) + \text{CO}_2$  reactions below  $100 \text{ kcal mol}^{-1}$ . Geometries are optimized at the CCSD(T)/aug-cc-pVTZ level of theory. All structures are planar, with  $C_s$  symmetry, except for both  $\text{CO}_3$  structures and  $\text{TS1}(^3A')$ , which have  $C_{2v}$  symmetry. Bond angles are rounded to the nearest degree.

Table S1 also lists the coupled cluster  $T_1$ <sup>44</sup> and  $D_1$  diagnostics.<sup>45</sup> However, the energy-based %TAEe[(T)] diagnostic has been found to provide a better correlation with the magnitude of post-CCSD(T) contributions than the  $T_1$  and  $D_1$  diagnostics (see refs 40 and 43 for further details). The trioxxygen species considered in the present study exhibit moderate nondynamical correlation effects; 44–54% of the atomization energy is accounted for at the SCF level, and 5–7% by the (T) contribution.

The computational protocol of W4 theory has been specified and rationalized in ref 40. There are two minor differences in the present work: (1) the reference geometries were optimized at the CCSD(T)/aug-cc-pVTZ level of theory rather than at the CCSD(T)/cc-pVQZ level of theory, and (2) for the tetratomic systems with  $C_s$  symmetry, the CCSDTQ5 calculations are approximated as CCSDTQ(5)<sub>A</sub>; this approximation has been justified in ref 42. Benchmark calculations of the W4 theory have been tested on the  $\text{O}(^3P) + \text{HCl}$  system, and the results can be found in SI.

Table 1 gives the final zero-point exclusive, nonrelativistic, clamped-nuclei W4 CCSD(T) and FCI basis set limits for the species in Figure 1. For all the systems, the CCSD(T)/aug-cc-pVTZ energies are within  $0.7 \text{ kcal mol}^{-1}$  of the W4 CCSD(T) basis set limits, where the largest deviation is found for the TS3 system. Table 2 presents the component breakdown for the W4 atomization energies as well as for the relevant reaction energies and barrier heights. Post-CCSD(T) contributions are found to be quite significant for the tetratomic systems TS1–TS3 and for  $\text{CO}_3$ . The contributions from the connected quadruple excitations increase the atomization energies by amounts ranging from  $1.8 \text{ kcal mol}^{-1}$  in TS1 to  $3.4 \text{ kcal mol}^{-1}$  in  $\text{CO}_3$ . The noniterative quintuple contributions further increase the atomization energies by  $0.1$ – $0.3 \text{ kcal mol}^{-1}$ , where again the highest contribution is seen for  $\text{CO}_3$ . The higher-order triples,  $T_3$ –(T), have contributions that reduce the atomization energies by  $0.3$ – $0.7 \text{ kcal mol}^{-1}$  for TS1–TS3 and increase the atomization energies by  $0.2 \text{ kcal mol}^{-1}$  for  $\text{CO}_3$ . Overall, post-CCSD(T)

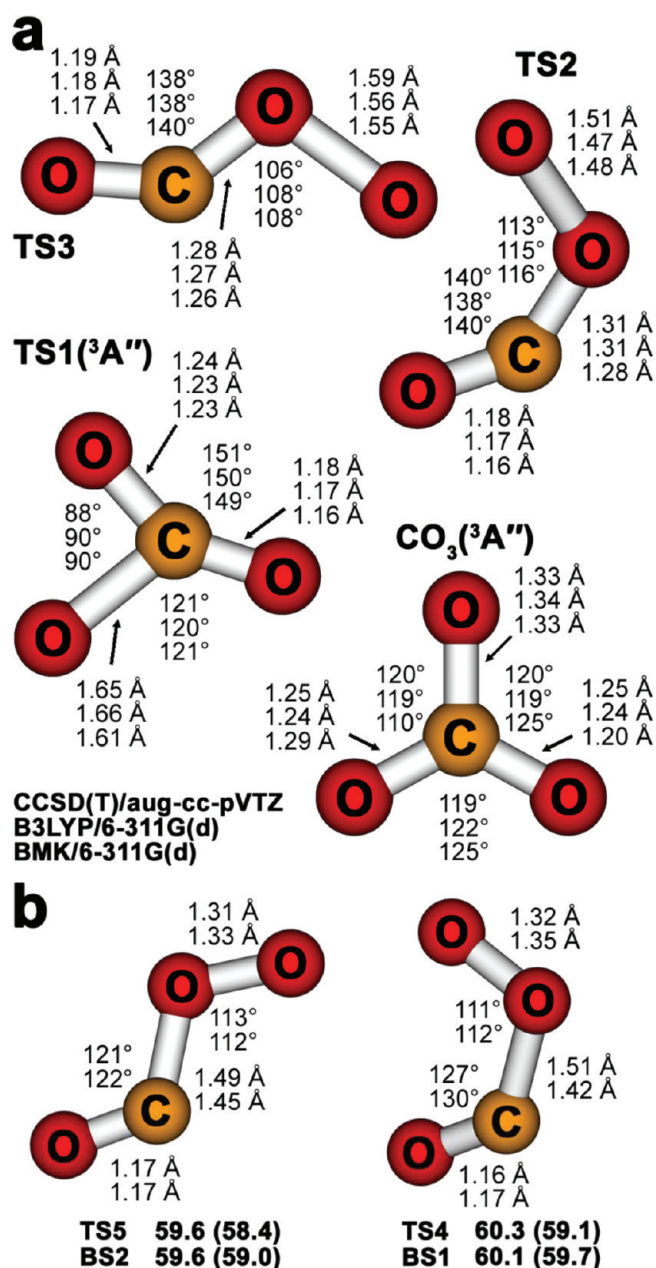


**Figure 2.** (a) Comparison of the lowest-energy stationary point geometries relevant to the QCT calculations. Geometries optimized at the CCSD(T)/aug-cc-pVTZ, B3LYP/6-311G(d), and BMK/6-311G(d) levels of theory are shown. (b) The remaining stationary points associated with the oxygen-atom abstraction reaction at the CCSD(T)/aug-cc-pVTZ level of theory. The calculated energies are shown below each structure in  $\text{kcal mol}^{-1}$ , with the ZPE-corrected values in parentheses.

contributions are found to be chemically significant for all of the tetratomic species; specifically, they increase the atomization energies of TS1, TS2, TS3, and  $\text{CO}_3$  by 1.5, 1.4, 2.2, and  $3.9 \text{ kcal mol}^{-1}$ , respectively.

Considering the reaction energies and barrier heights in the lower portion of Table 2, we note that both the  $T_3$ –(T) and  $T_4$  contributions are chemically significant, reaching up to  $2.3 \text{ kcal mol}^{-1}$  for  $\text{CO}_3$ . Furthermore, they both reduce the relative energies in nearly all of the cases, that is, there is mutual

**Table 1. Energies (kcal mol<sup>-1</sup>, Relative to the Free Reactants) for the Stationary Points on the Lowest Triplet CO<sub>3</sub> Potential Energy Surfaces for <sup>16</sup>O(<sup>3</sup>P) + <sup>12</sup>C<sup>16</sup>O<sub>2</sub> Collisions<sup>e</sup>**

	B3LYP/6-311G(d)		BMK/6-311G(d)		CCSD(T)/aug-cc-pVTZ		W4 CCSD(T) limit <sup>b</sup>	W4 FCI limit <sup>c</sup>	W4 FCI limit <sup>d</sup>
	w/ZPEC <sup>a</sup>		w/ZPEC <sup>a</sup>		w/ZPEC <sup>a</sup>				
TS1 ( <sup>3</sup> A'')	18.0	17.7	25.2	25.0	25.3	25.0	25.16	23.74	24.08
TS1 ( <sup>3</sup> A')					28.0	27.0			26.77
CO <sub>3</sub> ( <sup>3</sup> A'')	11.8	11.3	20.2	19.0	20.5	20.3	19.86	16.05	16.32
CO <sub>3</sub> ( <sup>3</sup> A')					18.2	18.0			16.39
TS2	56.2	55.2	65.3	64.5	63.0	62.1	63.05	61.75	62.27
TS3	70.3	69.2	80.0	78.9	76.5	75.3	77.12	75.01	75.44
O <sub>2</sub> + CO	9.7	7.9	14.3	12.6	10.3	8.3	9.89	9.25	9.87

<sup>a</sup> Zero-point-energy correction (ZPEC). <sup>b</sup> W4 zero-point exclusive, nonrelativistic, clamped-nuclei, valence CCSD(T) basis set limit. <sup>c</sup> W4 zero-point exclusive, nonrelativistic, clamped-nuclei, valence FCI basis set limit. <sup>d</sup> W4 zero-point exclusive, nonrelativistic, clamped-nuclei, all-electron FCI basis set limit for comparison with the DFT results. <sup>e</sup> The <sup>3</sup>A'' surface is lowest in all regions of the O(<sup>3</sup>P) + CO<sub>2</sub> PES that we examined, according to the W4 FCI-limit<sup>d</sup> level of theory.

**Table 2. Component Breakdown of the Final W4 Energies (kcal mol<sup>-1</sup>) at the Bottom of the Well**

	SCF	valence CCSD	valence (T)	T <sub>3</sub> -(T)	T <sub>4</sub>	T <sub>5</sub> <sup>a</sup>	inner-shell	relativistic	spin-orbit	DBOC	M-A <sup>b</sup>	TAE <sub>e</sub>
Total Atomization Energies												
O <sub>2</sub>	24.21	85.77	9.71	-0.77	1.26	0.12	0.17	-0.17	-0.45	0.01	0.03	119.88
CO	181.13	69.39	8.11	-0.56	0.62	0.03	0.93	-0.16	-0.31	0.02	0.04	259.21
CO <sub>2</sub>	257.34	116.85	14.02	-1.04	1.06	0.03	1.72	-0.48	-0.53	0.05	0.07	389.05
CO <sub>3</sub> ( <sup>3</sup> A')	201.69	150.50	18.63	-0.72	1.91	0.13	1.47	-0.54	-0.75	-0.11	0.08	372.25
CO <sub>3</sub> ( <sup>3</sup> A'')	189.59	157.59	21.17	0.22	3.38	0.28	1.45	-0.54	-0.75	0.01	0.08	372.44
TS1( <sup>3</sup> A')	188.82	151.21	20.68	-0.72	1.71	0.13	1.37	-0.48	-0.75	-0.06	0.07	361.98
TS1( <sup>3</sup> A'')	199.89	143.29	19.88	-0.43	1.82	0.11	1.40	-0.48	-0.75	0.01	0.07	364.75
TS2( <sup>3</sup> A'')	152.17	153.16	19.83	-0.67	1.94	0.12	1.20	-0.41	-0.75	0.00	0.08	326.62
TS3( <sup>3</sup> A'')	136.19	154.20	20.70	-0.25	2.31	0.12	1.29	-0.44	-0.75	0.01	0.08	313.43
Reaction Energies												
CO <sub>2</sub> + O → CO <sub>3</sub> ( <sup>3</sup> A'')	67.75	-40.74	-7.15	-1.26	-2.32	-0.25	0.26	0.06	0.22	0.03	-0.01	16.61
CO <sub>2</sub> + O → O <sub>2</sub> + CO	52.00	-38.31	-3.80	0.29	-0.81	-0.12	0.62	-0.15	0.22	0.02	-0.01	9.96
Forward Barriers												
CO <sub>2</sub> + O → TS1( <sup>3</sup> A'')	57.45	-26.44	-5.85	-0.61	-0.76	-0.05	0.34	-0.01	0.22	0.03	0.00	24.30
CO <sub>2</sub> + O → TS2( <sup>3</sup> A'')	105.17	-36.30	-5.81	-0.37	-0.87	-0.08	0.52	-0.08	0.22	0.04	-0.02	62.43
CO <sub>2</sub> + O → TS3( <sup>3</sup> A'')	121.14	-37.34	-6.68	-0.79	-1.25	-0.09	0.42	-0.04	0.22	0.04	-0.02	75.62
Reverse Barriers												
CO <sub>3</sub> ( <sup>3</sup> A'') → TS1( <sup>3</sup> A'')	-10.30	14.30	1.29	0.65	1.56	0.17	0.1	-0.1	0.00	0.0	0.01	7.69
O <sub>2</sub> + CO → TS2( <sup>3</sup> A'')	53.17	2.00	-2.01	-0.65	-0.06	0.04	-0.11	0.07	0.00	0.03	-0.01	52.47
O <sub>2</sub> + CO → TS3( <sup>3</sup> A'')	69.15	0.96	-2.88	-1.08	-0.44	0.03	-0.20	0.10	0.00	0.02	-0.01	65.66

<sup>a</sup> For TS1, TS2, TS3, and CO<sub>3</sub>(<sup>3</sup>A'), T<sub>5</sub> = CCSDTQ(5)<sub>T</sub>/cc-pVDZ(no d) - CCSDTQ/cc-pVDZ(no d). <sup>b</sup> Difference between the MOLPRO and ACES II definitions of the valence ROCCSD(T); one-half of this contribution is added to the final TAE as discussed in the appendix of reference 40.

amplification, rather than the typical cancellation, between the connected quadruples and the higher order triples contributions. Generally, the quintuple T<sub>5</sub> excitations reduce the relative energies by 0.1–0.2 kcal mol<sup>-1</sup> (one exception being the reverse barrier for the CO<sub>2</sub> + O → CO<sub>3</sub> reaction, for which T<sub>5</sub> excitations increase the barrier by 0.2 kcal mol<sup>-1</sup>). Overall, the post-CCSD(T) contributions reduce the reaction energies and barrier heights by 0.6–3.8 kcal mol<sup>-1</sup>, where the largest contribution is found for the reaction energy of the CO<sub>2</sub> + O → CO<sub>3</sub> reaction. The inner-shell correlation contributions vary in absolute value between 0.0–0.6 kcal mol<sup>-1</sup>, and the Darwin and mass-velocity scalar relativistic effects are on the order of 0.1 kcal mol<sup>-1</sup> in

absolute value. The diagonal Born–Oppenheimer corrections (DBOC) are found to be negligible for these reaction energies and barrier heights.

All but two of the structures [TS1(<sup>3</sup>A'') and CO<sub>3</sub>(<sup>3</sup>A'')] described in Figures 1 and 2 and Table 1 were previously characterized up to the MP2/6-31G\* level by Froese and Goddard.<sup>5</sup> Our coupled-cluster calculations show key differences. First, we found the <sup>3</sup>A'' surface to be lowest at the best W4 level of theory in all regions of the PES where we report stationary points. In contrast, at the MP2/6-31G\* level, the <sup>3</sup>A' surface was found to be the lowest near TS1 and CO<sub>3</sub>. However, at the W4 FCI-limit theory level, the lowest energy <sup>3</sup>A' surface is

very close in energy, in the vicinity of TS1 and CO<sub>3</sub>. The analogous structures have energies that are 2.69 and 0.07 kcal mol<sup>-1</sup> higher, respectively, on the <sup>3</sup>A' surface. Second, we found that neither BS1 nor BS2 is bound when zero-point energy (ZPE) is included, according to CCSD(T)/aug-cc-pVTZ. Thus, BS1, BS2, TS4, and TS5 are not as important as the other stationary points presented in this paper.

Several methods for direct dynamics were examined. The density-functional theory (DFT) methods, B3LYP/6-311G(d) and BMK/6-311G(d), were found to offer a good balance between computational cost and accuracy. They will not provide an accurate representation of nonadiabatic dynamics, however, because they are expected to converge to the lowest surface regardless of the associated wave function symmetry of that surface. Nonadiabatic dynamics might be important for this system, in the region of the PES near CO<sub>3</sub> and TS1, according to the CCSD(T)/aug-cc-pVTZ calculations, but the lowest <sup>3</sup>A'' and <sup>3</sup>A' surfaces appear sufficiently similar in the region where they are close in energy, such that DFT direct-dynamics calculations should still provide some insight into the reaction mechanisms.

The DFT methods predict stationary-point geometries that are close to those predicted by CCSD(T)/aug-cc-pVTZ (see Figure 2a). The BMK/6-311G(d) geometry, however, breaks the C<sub>2v</sub> symmetry of CO<sub>3</sub>. Both methods predict the stationary-point energies reasonably well, with BMK/6-311G(d) performing better on average (see Table 1). In particular, the B3LYP functional underestimates the W4 FCI basis set limit values, while the BMK functional overestimates them, albeit to a lesser extent. For CO<sub>3</sub>, TS1, TS2, and TS3, B3LYP underestimates the FCI limits by 4.5–6.1 kcal mol<sup>-1</sup> and BMK overestimates them by 1.1–4.6 kcal mol<sup>-1</sup>.

**B. Reaction Dynamics Calculations.** Direct dynamics calculations were run on the lowest triplet PES. They are based on forces and energies derived from B3LYP/6-311G(d) and BMK/6-311G(d) calculations performed using Q-Chem.<sup>38</sup> The initial orientation and impact parameter were sampled randomly. A CO<sub>2</sub> intramolecular trajectory was run with ZPE in each normal mode, facilitating the random sampling of the initial CO<sub>2</sub> vibrational phase. Trajectories were run at seven collision energies, shown in Table 3, between 23.1 and 149.9 kcal mol<sup>-1</sup>. A total of 400 trajectories were propagated for each collision energy and level of theory. No BMK-based trajectories were run with a collision energy of 23.1 kcal mol<sup>-1</sup> because this energy is insufficient for reaction at this theory level. Trajectories were integrated using a standard fifth-order predictor, sixth-order corrector integration algorithm<sup>46,47</sup> with an integration time-step of 10.0 au (0.24 fs), and they were stopped when the distance between any two atoms exceeded 12 a<sub>0</sub> (6.4 Å).

A maximum impact parameter for reactive scattering,  $b_{\max}$ , was estimated using<sup>48</sup>

$$b_{\max} = d(1 - E_0/E_{\text{coll}})^{1/2} \quad (3)$$

where  $d$  is the distance in the transition-state structure between the center of mass of the reactant CO<sub>2</sub> and the colliding oxygen atom,  $E_0$  is the transition-state energy, and  $E_{\text{coll}}$  is the collision energy. Because large collision energies were of principal interest, we chose to consider the largest value for  $b_{\max}$  suitable for trajectories with unlimited collision energy by setting  $E_{\text{coll}} = \infty$  in eq 3. Reaction 2 had the largest  $d$  values, with  $d \sim 4.3$  a<sub>0</sub> (2.3 Å) for both TS2 and TS3. This  $d$  value, combined with a

**Table 3. Number of Reactive QCTs Observed and Reactive Cross Sections Calculated at Different Collision Energies<sup>a</sup>**

collision energy (kcal mol <sup>-1</sup> )	oxygen isotope exchange				O-atom abstraction	
	B3LYP <sup>b</sup>		BMK <sup>b</sup>		B3LYP <sup>b</sup>	BMK <sup>b</sup>
	#	$\sigma$ (a <sub>0</sub> <sup>2</sup> ) <sup>c</sup>	#	$\sigma$ (a <sub>0</sub> <sup>2</sup> ) <sup>c</sup>	#	#
23.1	1	0.00143			0	
34.6	16	0.650	2	0.0552	0	0
57.7	54	4.57	37	2.51	0	0
80.7	66	6.45	66	5.52	0	0
103.8	68	6.87	80	7.12	1	0
126.8	80	8.52	76	7.72	4	5
149.9	78	8.33	80	8.01	11	8

<sup>a</sup> A total of 400 trajectories were propagated for each collision energy and level of theory. <sup>b</sup> Calculated with a 6-311G(d) basis set. <sup>c</sup>  $1 \text{ a}_0^2 = 2.80 \times 10^{-17} \text{ cm}^2$ .

~15% safety margin, suggested  $b_{\max} = 5.0 \text{ a}_0$  (2.6 Å); thus, the trajectories were sampled with impact parameters  $0 < b < 5.0 \text{ a}_0$ .

Energy conservation and spin contamination were checked at each time-step. Trajectories in which energy was not conserved to within 3 kcal mol<sup>-1</sup> or spin contamination rose above  $\langle S^2 \rangle = 2.5$  were flagged. Less than 1.3 and 10% of the B3LYP and BMK trajectories, respectively, failed to meet these criteria. Most problems were related to energy conservation, namely, self-consistent field (SCF) convergence to an excited electronic state. Trajectories that initially did not meet the criteria were run again using a different set of SCF convergence tools, which improved the energy-conservation or spin-contamination problem in many cases. Results of the rerun trajectories were compared to their initial-run analogues, and the one that met or came closest to meeting the acceptance criteria was included in the analysis. To do otherwise would have resulted in an underestimation of the reaction cross sections, as most of the problematic trajectories were reactive ones. These convergence and contamination problems may have had some impact on the statistics.

The total collision cross-section,  $\sigma_{\text{total}}$ , was estimated using the Lennard-Jones parameters for O and CO<sub>2</sub> according to the expression

$$\sigma_{\text{total}} = \pi b_{\text{total}}^2 \quad (4)$$

where  $b_{\text{total}}$  is the radius beyond which no elastic, inelastic, or reactive scattering occurs. This radius can be estimated using the Lennard-Jones potential:<sup>49</sup>

$$V(r) = 4\epsilon \left[ \left( \frac{\sigma(A)}{r} \right)^{12} - \left( \frac{\sigma(A)}{r} \right)^{-6} \right] \quad (5)$$

where  $\epsilon$  and  $\sigma(A)$  correspond to the well depth and the collision diameter, respectively, for an interaction between a pair of like atoms or molecules A. The collision diameter,  $\sigma(A)$ , is the distance where the potential crosses zero and is a measure of the atomic or molecular size. The values for the O atom and for CO<sub>2</sub> have been estimated to be  $\sigma(\text{O}) = 2.78 \text{ Å}$  and  $\sigma(\text{CO}_2) = 3.897 \text{ Å}$ , respectively.<sup>49,50</sup> These parameters can be combined using the rule<sup>51</sup>

$$\sigma(\text{O} + \text{CO}_2) = \frac{1}{2}[\sigma(\text{O}) + \sigma(\text{CO}_2)] \quad (6)$$

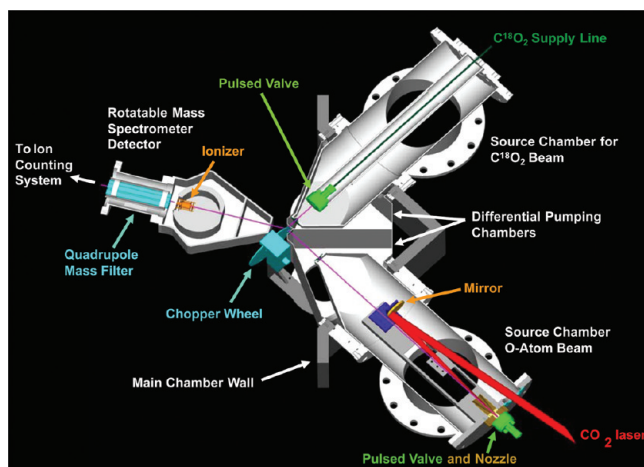


**Figure 3.** Crossed-molecular-beams apparatus with hyperthermal oxygen source.

which gives  $\sigma(\text{O} + \text{CO}_2) = 3.34 \text{ \AA}$ . Setting  $b_{\text{total}} = \sigma(\text{O} + \text{CO}_2)$  yields a cross section  $\sigma_{\text{total}} = 125.2 a_0^2 (6.625 \times 10^{-15} \text{ cm}^2)$ .

### III. EXPERIMENTAL METHODS

Crossed-molecular-beams experiments were performed using an apparatus equipped with a hyperthermal atomic-oxygen beam source at Montana State University, which has been described previously.<sup>52–55</sup> A diagram of the experimental setup is shown in Figure 3. A pulsed, hyperthermal beam of  $\sim 87\%$   $^{16}\text{O}(^3\text{P})$  and  $\sim 13\%$   $^{16}\text{O}_2(^3\Sigma_g^-)$  was generated by laser-induced detonation of  $^{16}\text{O}_2$  using a high-energy  $\text{CO}_2$  TEA laser ( $\sim 7 \text{ J pulse}^{-1}$ ) operating at a pulse repetition rate of 2 Hz. Though the velocity distribution ( $6\text{--}9 \text{ km s}^{-1}$ ) of the beam was initially broad, a portion of the overall distribution was velocity-selected using a synchronized chopper wheel operating at 300 Hz. This beam was then crossed, at a nominal angle of  $90^\circ$ , with a pulsed supersonic beam of  $98\%$   $^{12}\text{C}^{18}\text{O}_2$  (Spectra Gases). The molecular beams and scattered products were detected with a rotatable quadrupole mass spectrometer employing electron-bombardment ionization<sup>56</sup> at 160 eV and a Daly-type ion counter.<sup>57</sup> Number-density distributions for each product as a function of arrival time at the ionizer,  $N(t)$ , were obtained with a multichannel scaler (MCS) over a range of laboratory angles ( $\Theta = 6\text{--}54^\circ$ ). Laboratory angles were defined relative to the direction of the incident hyperthermal oxygen beam (i.e.,  $\Theta = 0^\circ$ ), with an increasing value corresponding to the direction toward the  $\text{CO}_2$  beam propagation direction. The resulting time-of-flight (TOF) distributions for the 33.7 cm distance between the beam interaction region and the ionizer were integrated to obtain angular distributions of scattered products in the laboratory frame,  $N(\Theta)$ .

In these experiments, the average velocity of the hyperthermal oxygen beam was  $8262 \pm 450 \text{ m s}^{-1}$  (i.e.,  $900 \text{ m s}^{-1}$  full width at half-maximum; fwhm), which corresponds to average laboratory-frame translational energies of  $130.5 \pm 14 \text{ kcal mol}^{-1}$  for  $^{16}\text{O}(^3\text{P})$ . The relative amounts of atomic ( $\sim 87\%$ ) and molecular ( $\sim 13\%$ ) oxygen were determined by integrating the TOF distributions at  $m/z = 16$  ( $^{16}\text{O}^+$ ) and  $32$  ( $^{16}\text{O}_2^+$ ) at  $\Theta = 0^\circ$  and correcting for  $\text{O}_2$  fragmentation (11% of the  $m/z = 32$  signal) in the electron-bombardment ionization region.

Laboratory TOF product distributions were measured every  $2^\circ$  in the range  $\Theta = 6\text{--}54^\circ$ . When collecting TOF distributions

of scattered products, individual TOF distributions were first collected for many relevant mass-to-charge ratios at a given laboratory (detector) angle. Then, the angle was incremented  $2^\circ$  and another set of TOF distributions was collected for these mass-to-charge ratios, and so forth, until the entire angular range was covered. Finally, the increment direction was reversed, and the cycle was repeated until a total of six TOF distributions had been recorded for each mass-to-charge ratio corresponding to each laboratory angle. The six distributions for each mass-to-charge ratio at a given laboratory angle were summed to yield a TOF distribution whose relative magnitude and shape were minimally affected by long-term drifts in experimental parameters. Individual product TOF distributions were collected for 200 beam pulses for  $m/z = 16$  ( $^{16}\text{O}^+$ ) and  $32$  ( $^{16}\text{O}_2^+$ ), for 1000 beam pulses for  $m/z = 46$  ( $^{16}\text{O}^{12}\text{C}^{18}\text{O}^+$ ), and for 500 beam pulses for  $m/z = 48$  ( $^{12}\text{C}^{18}\text{O}_2^+$ ). In contrast to the way in which the TOF distributions were collected for  $m/z = 16, 32, 46,$  and  $48$ , scattered products at  $m/z = 34$  ( $^{18}\text{O}^{16}\text{O}^+$ ) were collected to produce two TOF distributions corresponding to  $\Theta = 6$  and  $10^\circ$ , each of which was accumulated for 6000 beam pulses. An additional TOF distribution was collected for  $m/z = 34$  at  $\Theta = 14^\circ$ ; this TOF distribution was collected for 12000 beam pulses. For all TOF distributions, the dwell time for each channel of the MCS was  $1 \mu\text{s}$ . With a representative laboratory angle of  $10^\circ$ , integrated count rates were  $1.1 \times 10^7 \text{ s}^{-1}$  for  $m/z = 16$  ( $^{16}\text{O}^+$ ),  $1.3 \times 10^7 \text{ s}^{-1}$  for  $m/z = 32$  ( $^{16}\text{O}_2^+$ ),  $1.4 \times 10^4 \text{ s}^{-1}$  for  $m/z = 34$  ( $^{18}\text{O}^{16}\text{O}^+$ ),  $1.8 \times 10^5 \text{ s}^{-1}$  for  $m/z = 46$  ( $^{16}\text{O}^{12}\text{C}^{18}\text{O}^+$ ), and  $4.2 \times 10^6 \text{ s}^{-1}$  for  $m/z = 48$  ( $^{12}\text{C}^{18}\text{O}_2^+$ ). Raw flight times were converted to flight times over the 33.7 cm distance between the interaction region and the electron-bombardment ionizer by subtracting the time between the pulsed valve trigger pulse and the  $\text{CO}_2$  laser pulse ( $174 \mu\text{s}$ ), an electronic latency time ( $3 \mu\text{s}$ ), the oxygen flight time from the nozzle to the interaction region ( $120 \mu\text{s}$ , corresponding to the average velocity of the hyperthermal oxygen beam), and finally, the ion flight time between the ionizer and the Daly ion counter. The ion flight time is given by  $\alpha(m/z)^{1/2}$ , where  $\alpha = 2.44$  in these experiments, determined by comparing the relative arrival times of hyperthermal O and  $\text{O}_2$  at the detector.<sup>54</sup> Some uncertainty arises in the product times-of-flight because the exact time and point-of-origin of the oxygen beam are not well-determined; we estimate this uncertainty to be  $\sim 2 \mu\text{s}$  because the laser pulse width in the hyperthermal oxygen source could be as long as  $1 \mu\text{s}$  (a 100 ns wide peak with a long tail).

Three signal corrections were made before data analysis. First, we corrected for divergence of the hyperthermal O-atom beam at  $\Theta = 6\text{--}16^\circ$ . The divergent intensity was measured by obtaining TOF distributions at  $m/z = 16$  and  $32$  from  $\Theta = 6\text{--}16^\circ$  with the  $^{12}\text{C}^{18}\text{O}_2$  beam turned off. These TOF distributions were then scaled and subtracted from the corresponding experimental TOF distributions at  $m/z = 16$  and  $32$ , collected when the  $^{12}\text{C}^{18}\text{O}_2$  beam was on. Uncertainties in the nonreactive and reactive scattering signals resulting from collisions of the divergent oxygen could not be quantified. Instead, they were considered during the analysis of the laboratory data, where collisions at crossing angles of  $88, 89, 90, 91,$  and  $92^\circ$  were included during forward-convolution fitting. Including more crossing angles did not affect the forward-convolution fits significantly. Second, we corrected for the 2%  $^{16}\text{O}^{12}\text{C}^{18}\text{O}$  in the  $^{12}\text{C}^{18}\text{O}_2$  beam, a value we measured using the molecular-beam instrument's mass spectrometer. Thus, 2% of the inelastic scattering signal ( $m/z = 48$ ) at each laboratory angle ( $\Theta = 6\text{--}54^\circ$ ) was subtracted from raw  $m/z = 46$

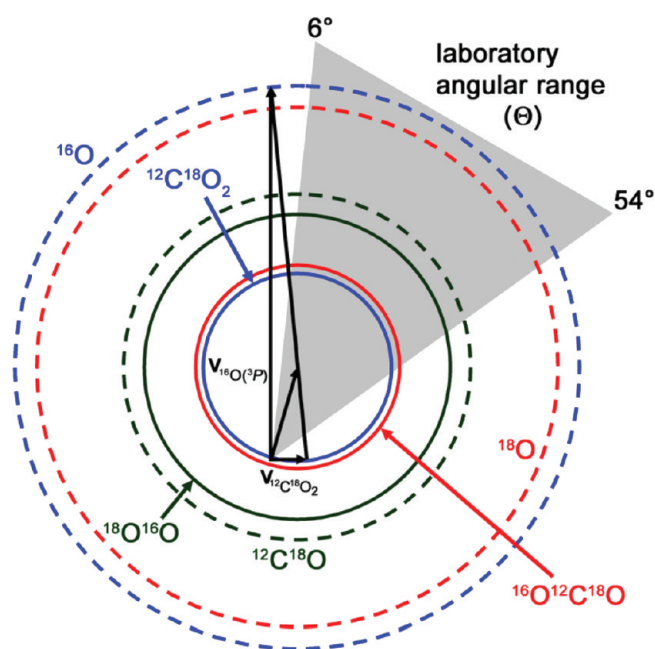


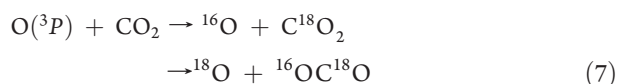
**Figure 4.** Newton diagram for  $^{16}\text{O}(^3P) + ^{12}\text{C}^{18}\text{O}_2$  collisions at  $E_{\text{coll}} = 98.8 \text{ kcal mol}^{-1}$ , where the  $^{16}\text{O}$ -atom beam velocity is  $8262 \text{ m s}^{-1}$  and the  $^{12}\text{C}^{18}\text{O}_2$  beam velocity is  $800 \text{ m s}^{-1}$ . The shaded region indicates the range of laboratory angles probed. The radii of the circles represent the maximum recoil velocities of the following products of  $^{16}\text{O}(^3P) + ^{12}\text{C}^{18}\text{O}_2$  collisions:  $^{12}\text{C}^{18}\text{O}_2$  (blue solid) +  $^{16}\text{O}$  (blue dashed),  $^{16}\text{O}^{12}\text{C}^{18}\text{O}$  (red solid) +  $^{18}\text{O}$  (red dashed), and  $^{18}\text{O}^{16}\text{O}$  (green solid) +  $^{12}\text{C}^{18}\text{O}$  (green dashed).

( $^{16}\text{O}^{12}\text{C}^{18}\text{O}^+$ ) TOF distributions. Finally, the hyperthermal  $\text{O}_2$  beam contained 0.4%  $^{18}\text{O}^{16}\text{O}$  (at natural isotopic abundances), so 0.4% of the nonreactive scattering signal ( $m/z = 34$ ) was subtracted from the raw  $m/z = 34$  ( $^{18}\text{O}^{16}\text{O}^+$ ) TOF distributions.

A forward-convolution method was used to derive c.m. translational energy  $P(E_T)$  and angular  $T(\theta_{\text{c.m.}})$  distributions from the resulting laboratory  $N(t)$  and  $N(\Theta)$  distributions.<sup>54,58</sup> Details of the LAB-to-c.m. transformation and fitting procedure are given in the SI. The Newton diagram used in this analysis is shown in Figure 4. The center-of-mass angle  $\theta_{\text{c.m.}} = 0^\circ$  (forward scattering) is defined as the initial c.m. direction of the O-atom velocity and opposite to that of the  $\text{CO}_2$  c.m. velocity ( $\theta_{\text{c.m.}} = 180^\circ$ , backward scattering).

#### IV. RESULTS AND ANALYSIS

Products from nonreactive scattering, isotope exchange (7), and O-atom abstraction (8)



were all observed in the crossed-molecular-beams experiment. Because the hyperthermal oxygen beam contained approximately 13%  $\text{O}_2$ , some of the signal detected at all of the product  $m/z$  ratios arose from elastic, inelastic, or reactive scattering of  $\text{O}_2$  with  $\text{CO}_2$ . The  $\text{O}_2$  molecules have the same laboratory velocity as the O atoms and thus collide with  $\text{CO}_2$  at a significantly higher

c.m. collision energy ( $158 \text{ kcal mol}^{-1}$ ). The resulting differences in kinematics allowed us to analyze the  $\text{O}_2 + \text{CO}_2$  scattering independently and thus resolve the contributions of  $\text{O}_2 + \text{CO}_2$  collisions from those of  $\text{O} + \text{CO}_2$  collisions. The results of  $\text{O}_2 + \text{CO}_2$  elastic and inelastic scattering, which were detected as  $^{16}\text{O}_2$  and  $^{16}\text{O}^{18}\text{O}$ , are given in SI. The results from this data set on the isotope exchange reaction from collisions of  $\text{O}_2$  with  $\text{CO}_2$ , detected as  $^{16}\text{O}^{12}\text{C}^{18}\text{O}$  products, have been reported earlier.<sup>59</sup>

**A. Nonreactive Scattering of  $^{16}\text{O}$  and  $^{12}\text{C}^{18}\text{O}_2$ .** Elastically and inelastically scattered products were detected at  $m/z = 16(^{16}\text{O}^+)$  and  $48(^{12}\text{C}^{18}\text{O}_2)$ , respectively. As a result of the limits on the observed laboratory angular distribution, each of the two products sampled largely different ranges of the c.m. scattering angle. The two resulting sets of c.m. distributions cannot be momentum-matched, but they do provide complementary information.

O-atoms were detected in the forward direction, allowing the detection of most of the incoming oxygen atoms which scattered with little deflection from their initial direction by both elastic and large-impact-parameter inelastic scattering. These channels could not be resolved at small scattering angles; thus, elastically and inelastically scattered O atoms will be referred to collectively as “scattered  $^{16}\text{O}$ .”

The laboratory-frame TOF distributions,  $N(t)$ , and angular distribution,  $N(\Theta)$ , of the O-atoms detected at  $m/z = 16$  are shown in Figure 5. The resulting total c.m. translational energy distribution,  $P(E_T)$ , and angular distribution,  $T(\theta_{\text{c.m.}})$ , derived from these data are also shown in Figure 5. The forward peak in the c.m. angular distribution for scattered  $^{16}\text{O}$  at  $\theta_{\text{c.m.}} \sim 0^\circ$  is an extrapolation, because the high background from the hyperthermal oxygen source at small laboratory angles precludes measurements at these angles.<sup>60</sup> Scattered  $^{16}\text{O}$  had  $85.6 \text{ kcal mol}^{-1}$  translational energy (87% of the total initial energy), on average, with a  $P(E_T)$  distribution peaked at  $\sim 97 \text{ kcal mol}^{-1}$ . The  $T(\theta_{\text{c.m.}})$  distribution was highly peaked in the forward direction, with little scattered intensity for  $\theta_{\text{c.m.}} > 20^\circ$ . The c.m. angular range for  $^{16}\text{O}$  detection was limited (see Figure 4), however, so backward-scattered products were not detected. A TOF signal was observed at long flight times, especially at larger laboratory and c.m. angles (e.g.,  $\Theta = 20, 30,$  and  $40^\circ$  in Figure 5a), indicating some dependence of  $P(E_T)$  on  $T(\theta_{\text{c.m.}})$  with slower products appearing at larger c.m. angles; this effect was more evident in the data of the scattered  $^{12}\text{C}^{18}\text{O}_2$  cofragment.

The TOF distributions of nonreactively scattered  $^{12}\text{C}^{18}\text{O}_2$  are shown in Figure 6a. Given the range of laboratory angles (Figure 4), the experiment mainly detected  $^{12}\text{C}^{18}\text{O}_2$  scattered opposite to its initial direction in the c.m. frame (see Figures 4, 6, and 7). The TOF distributions were bimodal. We assigned the faster (short-flight-time) component in the TOF distributions to inelastically scattered  $^{12}\text{C}^{18}\text{O}_2$  products from  $^{16}\text{O}_2 + ^{12}\text{C}^{18}\text{O}_2$  collisions and the slower component to products from  $^{16}\text{O} + ^{12}\text{C}^{18}\text{O}_2$  collisions. Simultaneous forward convolution of both scattering processes led to fits of the TOF distributions and laboratory angular distributions. The resulting  $P(E_T)$  and  $T(\theta_{\text{c.m.}})$  distributions for O +  $\text{CO}_2$  scattering are shown in Figure 6, while the  $P(E_T)$  and  $T(\theta_{\text{c.m.}})$  distributions for the  $\text{O}_2 + \text{CO}_2$  scattering are presented in SI.

The  $P(E_T)$  distribution for  $^{16}\text{O} + ^{12}\text{C}^{18}\text{O}_2$  nonreactive scattering derived from the  $^{12}\text{C}^{18}\text{O}_2$  product TOF distributions was both broader and lower in energy, on average, than that obtained from the  $^{16}\text{O}$  TOF distributions. Our analysis of inelastically scattered  $^{12}\text{C}^{18}\text{O}_2$  molecules, however, indicated that one pair of  $P(E_T)$  and  $T(\theta_{\text{c.m.}})$  distributions was insufficient to simulate the

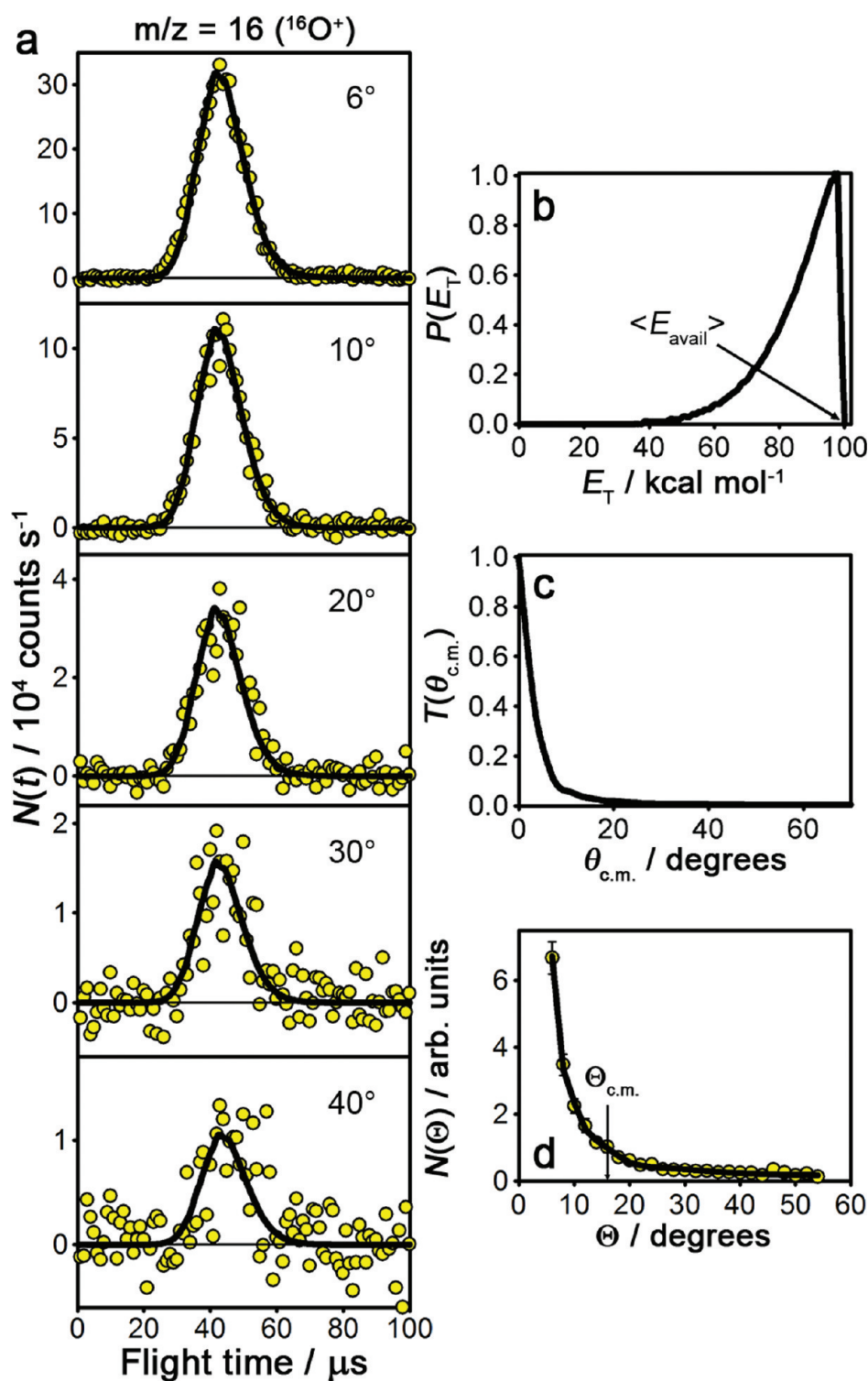


**Figure 5.** (a) Laboratory TOF, (b) c.m. translational energy, and (c) c.m. and (d) laboratory angular distributions for scattered  $^{16}\text{O}$  products from  $^{16}\text{O}(^3P) + ^{12}\text{C}^{18}\text{O}_2$  collisions at  $(E_{\text{coll}}) = 98.8 \text{ kcal mol}^{-1}$ . The translational energy distribution in (b) pertains to the total energy in translation of both  $^{16}\text{O}(^3P)$  and  $^{12}\text{C}^{18}\text{O}_2$ . The circles in (a) and (d) are experimental data, while the lines are the best-fit forward-convolution simulations of the experimental data derived from the c.m. translational energy and angular distributions shown in (b) and (c), respectively. The error bars in (d) represent  $2\sigma$  uncertainties in the integrated experimental TOF distributions (see Appendix A).

laboratory data accurately. This observation corresponds to a breakdown of the assumption that the c.m. angular and translational energy distributions are separable. Therefore, a second pair of

$P(E_T)$  and  $T(\theta_{\text{c.m.}})$  distributions was included in the fit of the  $^{12}\text{C}^{18}\text{O}_2$  TOF distributions (see Figure 6). The first pair of  $P(E_T)$  and  $T(\theta_{\text{c.m.}})$  distributions described the scattering at  $\theta_{\text{c.m.}} < 120^\circ$ .

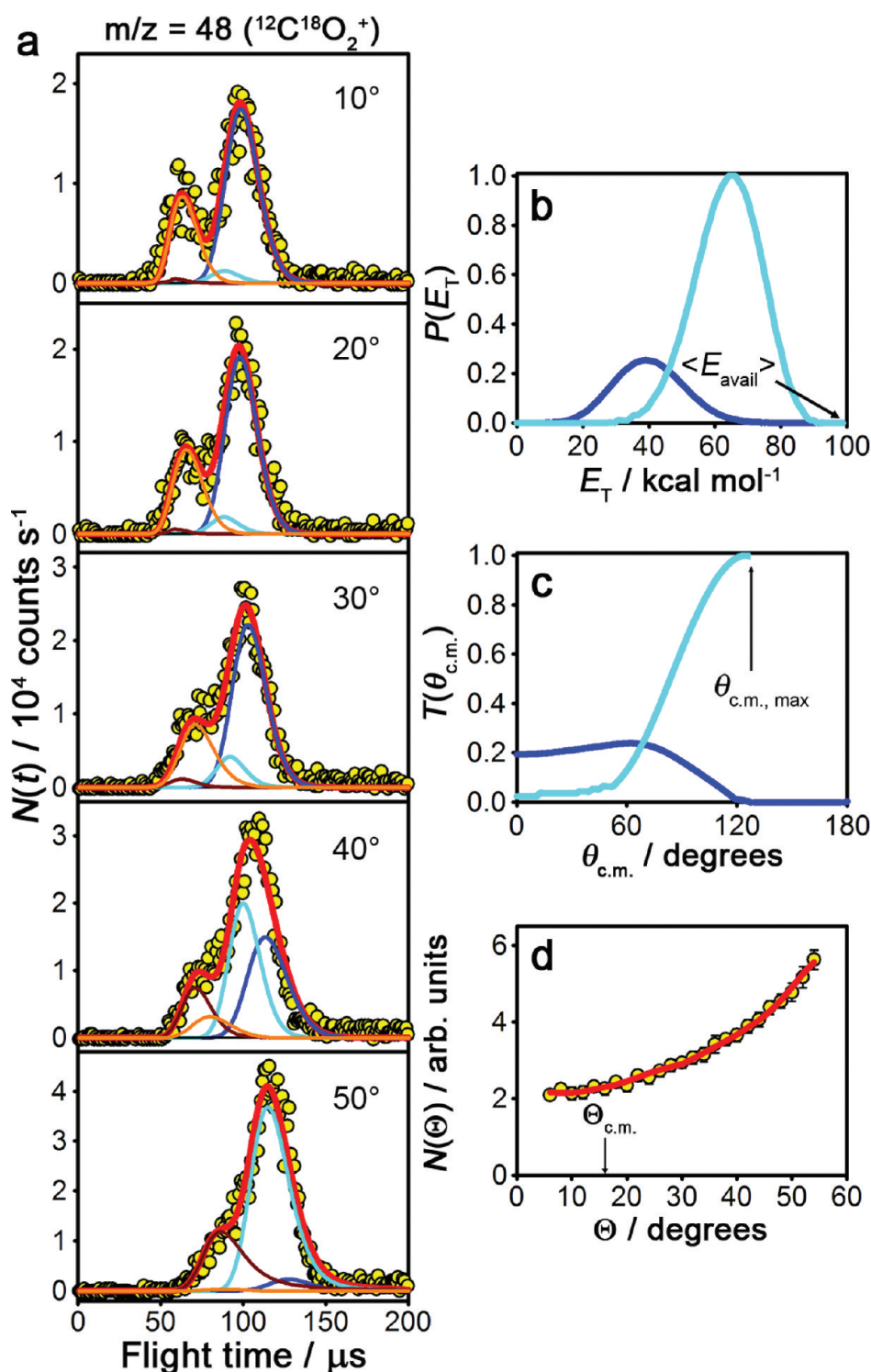


**Figure 6.** (a) Laboratory TOF, (b) c.m. translational energy, and (c) c.m. and (d) laboratory angular distributions for inelastically scattered  $^{12}\text{C}^{18}\text{O}_2$  products from  $^{16}\text{O}(^3P) + ^{12}\text{C}^{18}\text{O}_2$  collisions at  $\langle E_{\text{coll}} \rangle = 98.8 \text{ kcal mol}^{-1}$ . The circles in (a) and (d) are experimental data, while the lines (dark blue and cyan) are the best-fit forward-convolution simulations of the experimental data derived from the c.m. translational energy and angular distributions shown in (b) and (c), respectively; the maximum  $\theta_{\text{c.m.}}$  to which the experiment is sensitive is noted in (c). The error bars in (d) represent  $2\sigma$  uncertainties in the integrated experimental TOF distributions (see Appendix A). In (a), the fast components in the TOF distributions are inelastically scattered  $^{12}\text{C}^{18}\text{O}_2$  products from  $^{16}\text{O}_2 + ^{12}\text{C}^{18}\text{O}_2$  collisions at  $\langle E_{\text{coll}} \rangle = 158.1 \text{ kcal mol}^{-1}$ . The corresponding c.m. angular and translational energy distributions can be found in the SI (orange and brown lines).

In this region, the angular distribution was peaked near  $\theta_{\text{c.m.}} = 60^\circ$ , though the probability remained roughly constant for  $\theta_{\text{c.m.}} < 60^\circ$ .

It decayed steadily for  $\theta_{\text{c.m.}} > 60^\circ$ . The corresponding  $P(E_T)$  was peaked at  $39 \text{ kcal mol}^{-1}$  with an average energy in translation of

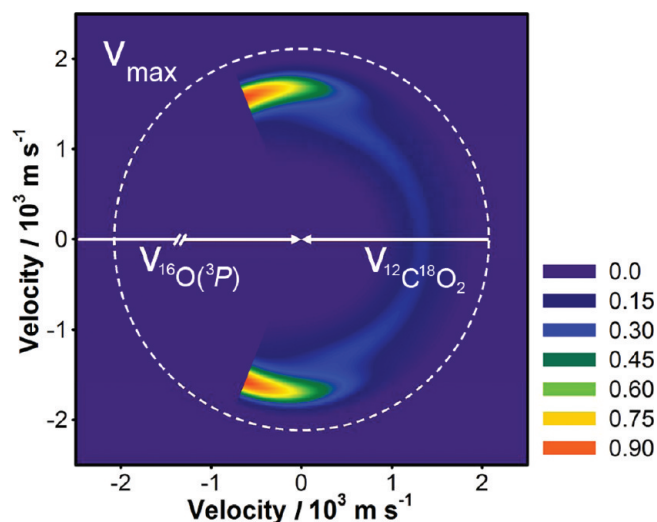


**Figure 7.** Velocity-flux contour diagram for inelastically scattered  $^{12}\text{C}^{18}\text{O}_2$  from  $^{16}\text{O}(^3P) + ^{12}\text{C}^{18}\text{O}_2$  collisions in the c.m. frame. The white arrows are the initial  $^{16}\text{O}(^3P)$  and  $^{12}\text{C}^{18}\text{O}_2$  velocity vectors, and the dashed white line is the maximum recoil velocity for  $^{12}\text{C}^{18}\text{O}_2$ . Only the c.m. angles for which the experiment was sensitive are shown.

$\langle E_T \rangle = 40.1 \text{ kcal mol}^{-1}$ , or 41% of the available energy. The other pair of  $P(E_T)$  and  $T(\theta_{\text{c.m.}})$  distributions described the scattering at  $60^\circ < \theta_{\text{c.m.}} < 125^\circ$ .  $\theta_{\text{c.m.}} = 125^\circ$  is the largest angle that was experimentally observable (see Figure 4). It should be noted, however, that the true c.m. angular distribution for  $^{12}\text{C}^{18}\text{O}_2$  undoubtedly increases sharply for  $\theta_{\text{c.m.}} > 120^\circ$ . The  $P(E_T)$  distribution derived from the  $^{12}\text{C}^{18}\text{O}_2$  TOF distributions had a maximum near  $65 \text{ kcal mol}^{-1}$ , with  $\langle E_T \rangle = 63.8 \text{ kcal mol}^{-1}$ , or 65% of the available energy.

The c.m. velocity-flux contour diagram for inelastically scattered  $^{12}\text{C}^{18}\text{O}_2$  is shown in Figure 7. The stronger and faster backward-scattering component rises with increasing angle but is restricted by the detectable angular range to  $\theta_{\text{c.m.}} < 125^\circ$ . The slower, forward-scattered component is essentially isotropic for  $\theta_{\text{c.m.}} < 60^\circ$ . Our use of two pairs of  $P(E_T)$  and  $T(\theta_{\text{c.m.}})$  distributions to fit the laboratory data is similar to previous studies in which nonreactive scattering of  $\text{Cl} + \text{C}_3\text{H}_8$  and hyperthermal  $\text{O}(^3P) + \text{C}_2\text{H}_6$  was investigated.<sup>55,61</sup>

Similar results were observed for nonreactive scattering of  $^{16}\text{O}_2$  from  $^{12}\text{C}^{18}\text{O}_2$  with a collision energy of  $158 \text{ kcal mol}^{-1}$  (see the related discussion in SI), though the  $P(E_T)$  is less sharply peaked. There is a similar broad angular distribution of slow  $^{12}\text{C}^{18}\text{O}_2$  products scattered in the forward direction, though the translational energy distribution peaks at higher  $E_T$ .

There were several sources of uncertainty in the experimental data and in the forward convolution. First, the broad  $\text{O}(^3P)$  velocity distribution in the experiment, and the resulting broad collision energy distribution, leads to broadening of the  $P(E_T)$  distribution and could mask an underlying structure in this distribution. Second, the presence of the  $\text{O}_2 + \text{CO}_2$  collisions renders the higher  $E_T$  portion of the  $P(E_T)$  less certain. Constraints from the backward-scattered component of the laboratory TOF distributions were also limited due to the  $t^{-3}$  dependence of the scattered product intensity in the laboratory-to-c.m.-frame Jacobian transformation (see SI), which reduces the instrument's sensitivity to backward-scattered products. Consequently, the angular distribution of products near  $\theta_{\text{c.m.}} = 180^\circ$  is less certain.

The results of QCT trajectories that lead to inelastic scattering are shown in Figures 8 and 9. The opacity functions for inelastic trajectories on both the B3LYP and BMK surfaces are similar (the lowest energy trajectories at  $23.1 \text{ kcal/mol}$  were not performed on the BMK surface). They are in the range  $0.05\text{--}0.15$ , extend to the maximum impact parameter sampled,  $b = 5 a_0$ , and appear not to decrease over this range. This last result is expected, as the maximum impact parameter is less than the collision diameter  $\sigma(\text{O} + \text{CO}_2) = 6.3 a_0$ . Thus, our calculations do not include all inelastic scattering trajectories and likely do not include a large number of large-impact-parameter trajectories that lead to small deflections, that is, forward-scattered O-atoms and backward-scattered  $\text{CO}_2$ . The opacity function also appears to have a bimodal distribution, peaking at  $1.7 a_0$  and  $3.3 a_0$ . At the lowest energies, the two distributions are roughly comparable; however, as the collision energy is increased, the smaller-impact-parameter component decreases, while the larger-impact-parameter opacity increases, reaching a limit at  $103 \text{ kcal mol}^{-1}$ .

The calculated c.m. angular and translational energy distributions for scattered  $^{16}\text{O}$  at  $103 \text{ kcal mol}^{-1}$  are compared in Figure 9 with the corresponding experimental distributions determined from the total scattered  $^{16}\text{O}$ . The theoretical and experimental data are in reasonably good agreement. The average translational energies were similar:  $\langle E_T \rangle = 85$  and  $86 \text{ kcal mol}^{-1}$  for B3LYP and BMK, respectively, versus  $85.6 \text{ kcal mol}^{-1}$  in the experiment. The computed angular distributions decrease rapidly with increasing scattering angle, similar to the experimental distribution. The calculated angular distributions are less highly peaked at small  $\theta_{\text{c.m.}}$  than the experimental  $T(\theta_{\text{c.m.}})$  distribution, but this discrepancy may not be significant. There are a number of systematic biases and uncertainties that contribute at small angles, including (1) the absence of QCT trajectories with impact parameters larger than  $5 a_0$ , (2) the inclusion of both elastic and inelastic scattering in the total scattered  $^{16}\text{O}$  signal, and (3) uncertainties in extrapolating the forward scattered experimental  $^{16}\text{O}$   $P(E_T)$  distribution at  $0^\circ$  from measurements at larger angles ( $\Theta \geq 6^\circ$ ).

**B. Isotope Exchange Reaction:**  $^{16}\text{O}(^3P) + ^{12}\text{C}^{18}\text{O}_2 \rightarrow ^{18}\text{O} + ^{16}\text{O}^{12}\text{C}^{18}\text{O}$ . Isotope exchange reactions were observed by detecting the  $^{16}\text{O}^{12}\text{C}^{18}\text{O}$  product at  $m/z = 46$ . As described above, this product arises from reactions of  $^{12}\text{C}^{18}\text{O}_2$  with both  $^{16}\text{O}$  and  $^{16}\text{O}_2$ . We assigned the fastest reactively scattered  $^{16}\text{O}^{12}\text{C}^{18}\text{O}$  products in these experiments to O-atom exchange reactions between  $^{16}\text{O}_2$  and  $^{12}\text{C}^{18}\text{O}_2$  occurring at  $E_{\text{coll}} \sim 160 \text{ kcal mol}^{-1}$ , because energy conservation would have been violated if these products had been assigned to isotope exchange collisions of  $^{16}\text{O}(^3P)$  with  $^{12}\text{C}^{18}\text{O}_2$ . The higher collision energy is a consequence of the larger mass of  $\text{O}_2$  relative to O. The remaining  $m/z = 46$  product signal is a result of  $\text{O}(^3P) + \text{CO}_2$  isotope exchange reactions. The analysis of the isotope exchange reaction with  $\text{O}_2$  was reported earlier.<sup>59</sup>

Five representative laboratory-frame TOF distributions for the  $^{16}\text{O}^{12}\text{C}^{18}\text{O}$  product are shown in Figure 10. The fits to the TOF distributions are decomposed into the contributions from the two reactions, exchange with O and with  $\text{O}_2$ . The laboratory angular distributions and the c.m. translational energy and angular distributions that are derived from the laboratory TOF and angular distributions are also shown in Figure 10. These distributions only pertain to the isotope exchange reaction with O. Figure 11 shows the corresponding experimental velocity-flux contour diagram for the  $^{16}\text{O}^{12}\text{C}^{18}\text{O}$  product.

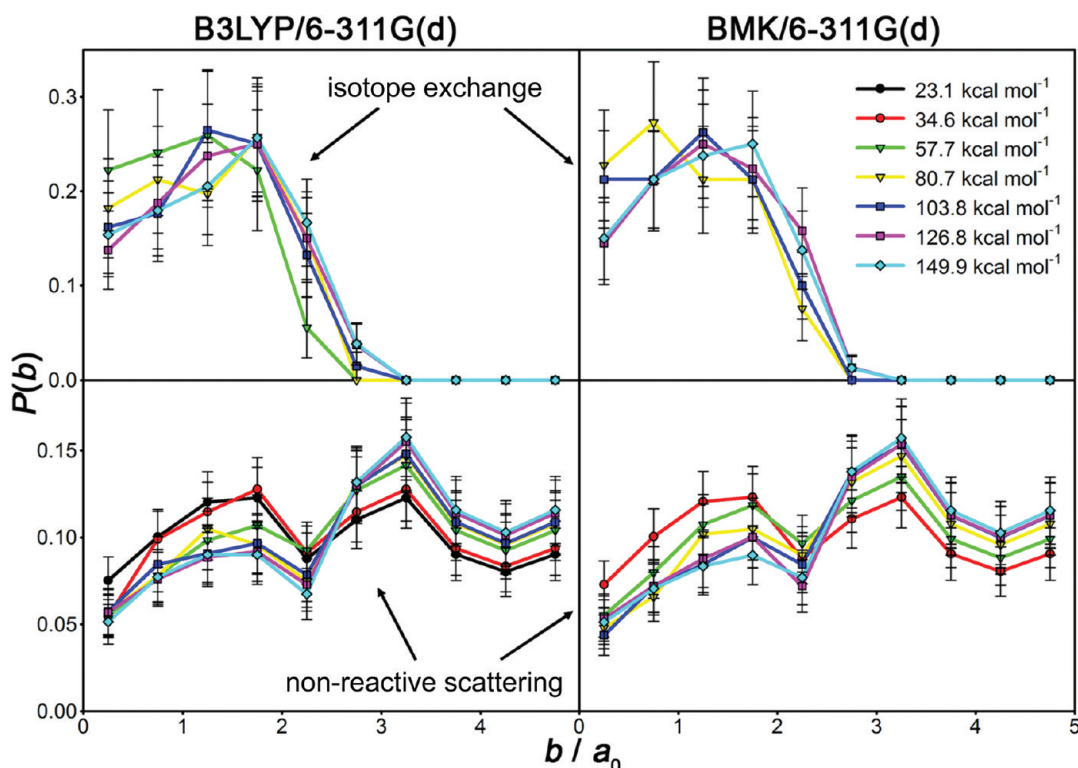


**Figure 8.** Opacity functions for the  $O(^3P) + CO_2$  isotope exchange reaction and for inelastic scattering obtained from the QCT calculations.

Laboratory data for  $O(^3P) + CO_2$  isotope exchange reactions at  $\langle E_{\text{coll}} \rangle = 98.8 \text{ kcal mol}^{-1}$  show a preference for backward scattering relative to the reagent oxygen atom direction (i.e., toward  $\theta_{\text{c.m.}} = 180^\circ$ ), with the isotopically exchanged products having relatively low translational energies ( $\langle E_T \rangle = 0.35E_{\text{avail}}$ ). Significant forward and sideways scattering of products was also observed in addition to backward scattering; the  $T(\theta_{\text{c.m.}})$  distribution indicates that products scattered in the range  $0^\circ < \theta_{\text{c.m.}} < 90^\circ$  do so with nearly equal probability, and that scattered products become increasingly more probable as  $\theta_{\text{c.m.}}$  approaches  $180^\circ$ . On average, the two products had  $34.8 \text{ kcal mol}^{-1}$  of total translational energy, with the  $P(E_T)$  distribution peaked at  $\sim 30 \text{ kcal mol}^{-1}$  (see Figure 10b).

Experimental uncertainties in the isotopic exchange data analysis are similar to those in the nonreactive scattering and include the broad velocity distribution of the hyperthermal  $O(^3P)$  beam, the presence of the  $O_2 + CO_2$  isotope exchange channel, which was not fully resolved from the forward-scattered  $^{16}O^{12}C^{18}O$  peak in the laboratory TOF and rendered the higher  $E_T$  portion of the  $P(E_T)$  distribution less certain, and uncertainty in the angular distribution of products near  $\theta_{\text{c.m.}} = 180^\circ$  resulting from reduced sensitivity of the backward-scattered component of the laboratory TOF distribution due to Jacobian factors.

Trajectories leading to isotope exchange were found in the QCT calculations above a threshold collision energy. Energy-dependent reaction cross sections for isotope exchange were calculated from the QCT data (see Table 3). These calculated excitation functions had the same shape at the B3LYP/6-311G(d) and BMK/6-311G(d) levels of theory, with the BMK result being slightly offset to higher energies relative to the B3LYP result. This offset is consistent with the  $7.3 \text{ kcal mol}^{-1}$  ( $0.32 \text{ eV}$ ) higher TS1 barrier for isotope exchange predicted by BMK. Opacity functions for the isotope exchange reaction,  $P(b)$ , are

shown in the upper panels of Figure 8; these functions computed on the two surfaces are similar. They appeared to reach a maximum of  $P(b) \sim 0.2$  at  $b \sim 1.5 a_0$ , with the peak becoming more prominent with increasing collision energy and shifting to slightly higher impact parameters. The maximum impact parameter is in qualitative agreement with our estimates from the line-of-centers model.

The theoretical  $T(\theta_{\text{c.m.}})$  and  $P(E_T)$  distributions derived from the QCT calculations at  $E_{\text{coll}} = 103.7 \text{ kcal mol}^{-1}$  are compared with the experimental data in Figure 12, where  $\langle E_{\text{coll}} \rangle = 98.8 \text{ kcal mol}^{-1}$ . The theoretical trajectories were summed into energy bins of  $\sim 11.5 \text{ kcal mol}^{-1}$ . Generally good agreement between experiment and theory was observed. Calculations at both levels of theory show a preference for backward-scattered  $^{16}O^{12}C^{18}O$  products. Both levels of theory predict a translational energy distribution that is peaked at relatively low energies with a long tail at higher energies. The experimental peak  $E_T$  ( $\sim 30 \text{ kcal mol}^{-1}$ ) lies somewhat below the most probable translational energies predicted by the QCT calculations ( $\sim 40 \text{ kcal mol}^{-1}$ ). The  $\langle E_T \rangle$  of  $34.8 \text{ kcal mol}^{-1}$  obtained from the experimental  $P(E_T)$  is somewhat less than those obtained from the B3LYP ( $\langle E_T \rangle = 43 \pm 15 \text{ kcal mol}^{-1}$ ) and BMK ( $\langle E_T \rangle = 47 \pm 16 \text{ kcal mol}^{-1}$ ) trajectories. Overall, the experimental and theoretical results both indicate that a significant amount of the collision energy is transferred to internal degrees of freedom during the  $O(^3P) + CO_2$  isotope exchange reaction. Uncertainty in the product translational energy distribution from the QCT data arises from the binning process used to obtain better statistics in the distribution; the width of each  $E_T$  bin was  $\sim 11.5 \text{ kcal mol}^{-1}$ , so disagreements in the  $P(E_T)$  peak locations between theory and experiment on the order of  $10 \text{ kcal mol}^{-1}$  are not unreasonable.

An examination of the trajectories revealed that during  $O(^3P) + CO_2$  collisions that resulted in oxygen isotope exchange, the

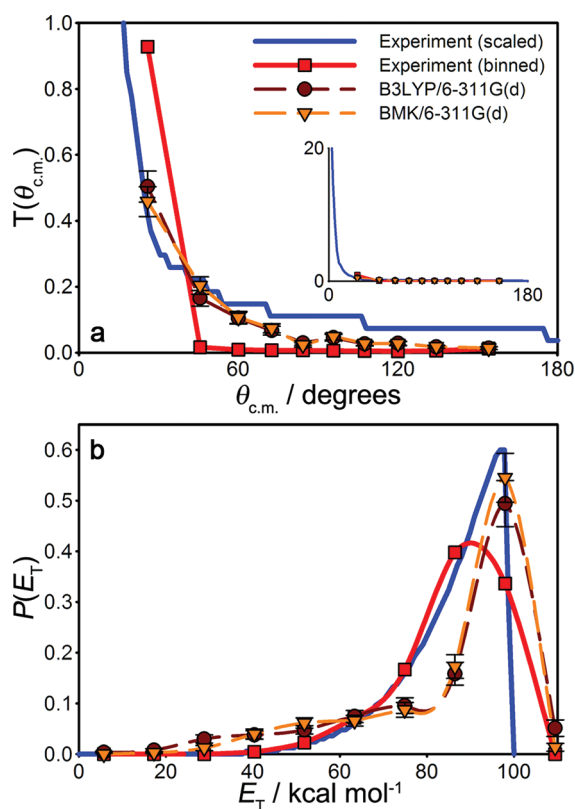


**Figure 9.** Comparison of laboratory and theoretical c.m. (a) angular and (b) translational energy distributions for nonreactive scattering of  $\text{O}(^3P)$  and  $\text{CO}_2$  at  $\langle E_{\text{coll}} \rangle \approx 100 \text{ kcal mol}^{-1}$ . Laboratory distributions are obtained from the scattered  $^{16}\text{O}$  data only (Figure 5). Distributions were binned using the bin midpoints shown here. The inset in the first panel shows the same data but with an expanded ordinate axis.

incoming oxygen atom interacted with the carbon atom on  $\text{CO}_2$  to form a  $\text{CO}_3^*$  complex (see Figure 13 and the sample trajectory animations in SI). In some cases, the  $\text{CO}_3^*$  complex existed for less than one vibrational period (the reaction is nearly direct), while in others it existed for several vibrational periods. After some time (typically  $\leq 200 \text{ fs}$ ), one of the oxygen atoms that was initially part of the  $\text{CO}_2$  detaches to leave behind a new  $\text{CO}_2$  molecule. Head-on collisions at higher collision energies tended to form complexes existing for shorter times than those formed similarly at lower energies. Higher energies also tended to form  $\text{CO}_3^*$  complexes that tumbled  $\geq 360^\circ$  in the plane of the reaction. In all cases, however, the  $\text{CO}_3^*$  complex lasted less than a picosecond. The preference for backward scattered O atoms results from direct collisions, in which the departing O atom is ejected in a displacement mechanism. Dissociation of an O atom from the complex otherwise has no angular preference.

**C. Oxygen-Atom Abstraction Reaction:**  $^{16}\text{O}(^3P) + ^{12}\text{C}^{18}\text{O}_2 \rightarrow ^{18}\text{O}^{16}\text{O} + ^{12}\text{C}^{18}\text{O}$ . Reactively scattered  $^{18}\text{O}^{16}\text{O}$  products detected at  $m/z = 34$  were clearly observable at  $\Theta = 6^\circ$ , barely detectable at  $\Theta = 10^\circ$ , and undetectable at  $\Theta = 14^\circ$  (see Figure 14). Due to the weak signal of  $^{18}\text{O}^{16}\text{O}$ , the TOF distributions were only collected at these three angles. While this laboratory-frame angular dependence may imply that  $^{18}\text{O}^{16}\text{O}$  products are mainly forward-scattered, we cannot rule out backward scattering because the experiment was not sensitive to it (see Figure 4). Therefore, the c.m. angular distribution is not reported here. The signal corresponding to the counter products at  $m/z = 30$

( $^{12}\text{C}^{18}\text{O}^+$ ) could not be observed because of high background signal from  $^{12}\text{C}^{18}\text{O}_2$  fragmentation in the ionizer. From the laboratory data, we obtained a product  $P(E_T)$  distribution peaked at  $56 \text{ kcal mol}^{-1}$ , indicating that  $^{18}\text{O}^{16}\text{O} + ^{12}\text{C}^{18}\text{O}$  products had  $55.0 \text{ kcal mol}^{-1}$  of translational energy, or 61% of the available energy, on average. No products were detected at  $m/z = 36$  ( $^{18}\text{O}_2^+$ ).

A very small number of trajectories in the QCT calculations led to  $\text{O}_2 + \text{CO}$  products. This channel opens at collision energies above  $100 \text{ kcal mol}^{-1}$ , significantly higher than the threshold for onset of the exchange channel (see Table 3), which is consistent with the higher transition-state barriers, TS2 and TS3, for the abstraction reaction. Because only a small number of these reactions were observed, the amount of mechanistic insight provided by the QCTs is somewhat limited. Essentially no trajectories resulted in oxygen-atom abstraction at the collision energy of the experiment, but there is no contradiction, as only 400 trajectories were run at any given energy.

In the QCT calculations at the B3LYP/6-311G(d) level of theory, 11 (out of 400) trajectories yielded  $\text{O}_2 + \text{CO}$  products at  $E_{\text{coll}} = 149.9 \text{ kcal mol}^{-1}$ . The reaction occurred in one of two ways: through a stripping-type mechanism or by way of a  $\text{CO}_3^*$  complex. In the stripping-type mechanism (see Figure 15a), the incoming oxygen atom interacts mainly with one of the oxygen atoms on  $\text{CO}_2$  to form TS3 directly. The C–O bond then breaks, releasing  $\text{O}_2 + \text{CO}$  products. Only two of these stripping-type trajectories were observed. The remaining nine trajectories, as well as all of the other trajectories that produced  $\text{O}_2 + \text{CO}$  at other collision energies or when BMK was used, proceeded through a  $\text{CO}_3^*$ -complex mechanism (see Figure 15b and example trajectories in SI). In that mechanism, the incoming oxygen atom interacted first with the carbon atom of  $\text{CO}_2$  to form a short-lived  $\text{CO}_3^*$  complex, which rarely survived more than one vibrational period. An oxygen atom was then released, subsequently interacting with a  $\text{CO}_2$ -bound oxygen atom as the  $\text{CO}_2$  rotated. The system then passed through a TS2-like structure as an O–O bond formed and the adjacent C–O bond broke to form  $\text{O}_2 + \text{CO}$  products.

The stripping-type mechanism would produce  $^{18}\text{O}^{16}\text{O}$  molecules exclusively, whereas the  $\text{CO}_3^*$ -complex mechanism can produce  $^{18}\text{O}_2$  in addition to  $^{18}\text{O}^{16}\text{O}$ . One of the 27 O-atom abstraction trajectories led to  $^{18}\text{O}^{16}\text{O}$  products, by way of a  $\text{CO}_3^*$ -complex mechanism. It is not possible to infer much from a single trajectory result, but it does indicate that such a process is viable. In the laboratory experiment, we did not observe any  $m/z = 36$  products, but our signal-to-noise ratio would almost certainly preclude detection of a channel that represented  $<5\%$  of the already weak O-atom abstraction signal at  $m/z = 34$ .

**D. Relative Product Yields.** Experimental relative product yields were calculated from the integrated cross sections for each channel, which were obtained from the forward-convolution simulations of the TOF data. Because the signal at  $m/z = 46$  contained contributions from both  $^{16}\text{O}(^3P) + ^{12}\text{C}^{18}\text{O}_2$  and  $^{16}\text{O}_2 + ^{12}\text{C}^{18}\text{O}_2$  collisions, the forward-convolution fits for  $^{16}\text{O}_2 + ^{12}\text{C}^{18}\text{O}_2$  isotope exchange were subtracted from the laboratory TOF data before the  $^{16}\text{O}(^3P) + ^{12}\text{C}^{18}\text{O}_2$  cross section was calculated. The resulting integrated cross sections were scaled by their electron-impact ionization cross sections and fragmentation patterns for the comparison. The transmission through the quadrupole mass filter was assumed to be the same for all the small molecules examined here. Using this method, we calculated branching fractions for nonreactive scattering (0.984), oxygen-atom abstraction ( $4 \times 10^{-6}$ ), and oxygen isotope exchange (0.016) based on the integrated cross sections obtained

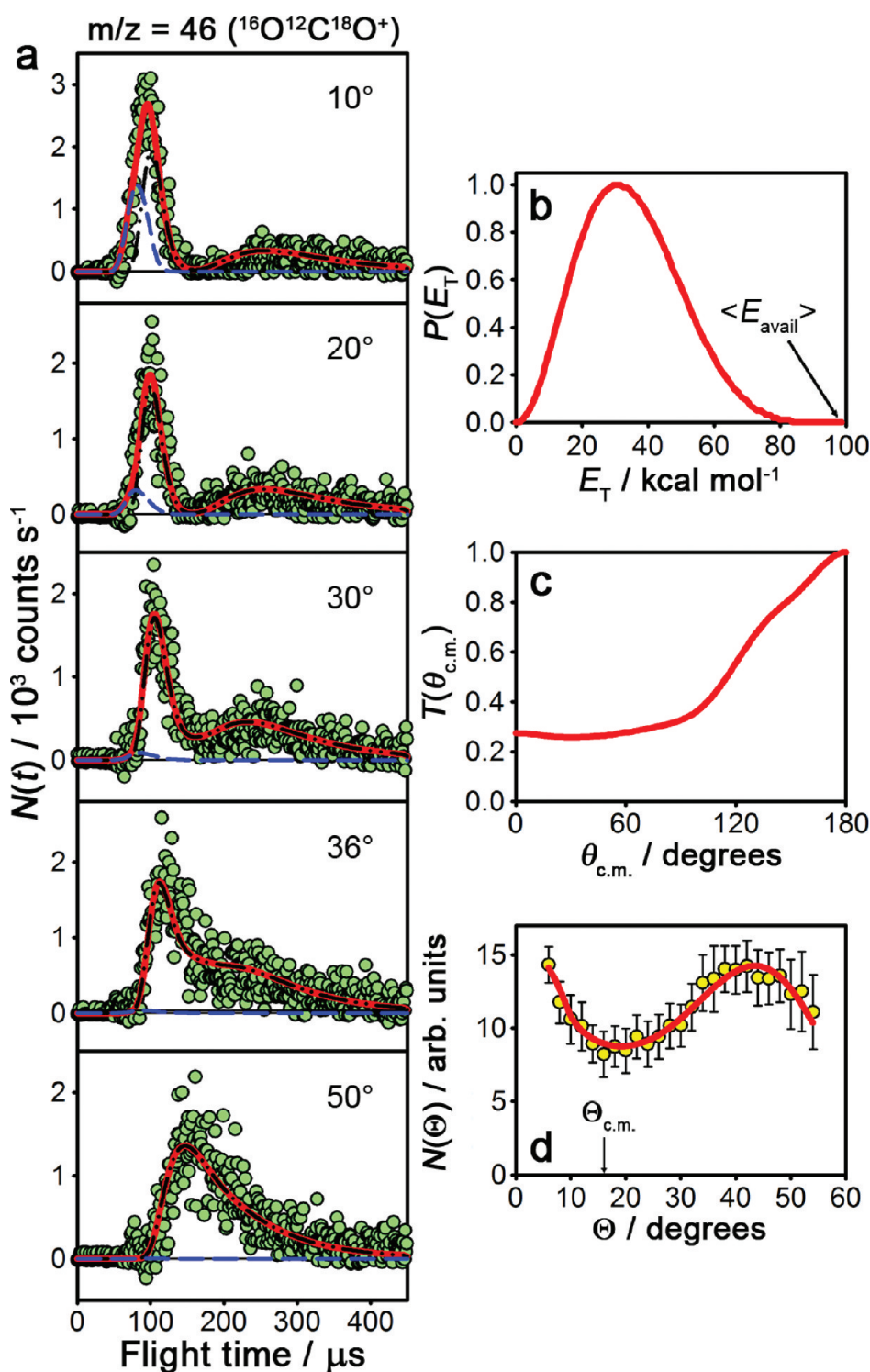


**Figure 10.** (a) Laboratory TOF, (b) c.m. translational energy, and (c) c.m. and (d) laboratory angular distributions for  $^{16}\text{O}^{12}\text{C}^{18}\text{O}$  products of the  $^{16}\text{O}(^3P) + ^{12}\text{C}^{18}\text{O}_2 \rightarrow ^{18}\text{O} + ^{16}\text{O}^{12}\text{C}^{18}\text{O}$  reaction at  $\langle E_{\text{coll}} \rangle = 98.8 \text{ kcal mol}^{-1}$ . The circles in (a) and (d) are experimental data, while the lines are the best-fit forward-convolution simulations of the experimental data derived from the c.m. translational energy and angular distributions shown in (b) and (c), respectively. In (a), the best-fit forward-convolution simulations of  $^{16}\text{O}^{12}\text{C}^{18}\text{O}$  products from  $^{16}\text{O}(^3P) + ^{12}\text{C}^{18}\text{O}_2$  collisions (black dot-dashed lines) are shown with those from  $^{16}\text{O}_2 + ^{12}\text{C}^{18}\text{O}_2$  collisions at  $\langle E_{\text{coll}} \rangle = 158.1 \text{ kcal mol}^{-1}$  (blue dashed lines).<sup>60</sup> The error bars in (d) represent  $2\sigma$  uncertainties in the integrated experimental TOF distributions (see Appendix A).

at  $m/z = 16, 34$ , and  $46$ , respectively. The accuracy of the laboratory-integrated cross sections depends on the accuracy of the best-fit c.m. angular and translational energy distributions. One

major uncertainty is in the need to extrapolate the magnitude of the large forward scattered  $^{16}\text{O}$  at angles  $\theta_{\text{c.m.}} < 4^\circ$ ; this should lead to uncertainties in the branching fraction of  $2\sigma = 0.05$

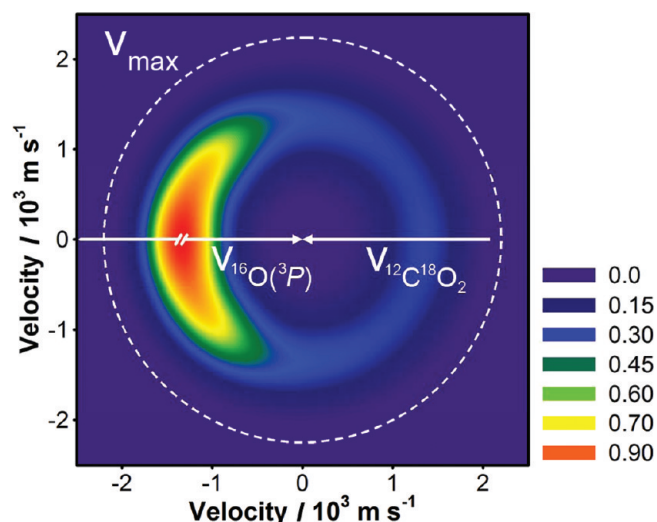


**Figure 11.** Velocity-flux contour diagram for  $^{16}\text{O}^{12}\text{C}^{18}\text{O}$  products from  $^{16}\text{O}(^3P) + ^{12}\text{C}^{18}\text{O}_2$  collisions in the c.m. frame. The white arrows are the initial  $^{16}\text{O}(^3P)$  and  $^{12}\text{C}^{18}\text{O}_2$  velocity vectors, and the dashed white line is the maximum recoil velocity for  $^{16}\text{O}^{12}\text{C}^{18}\text{O}$ .

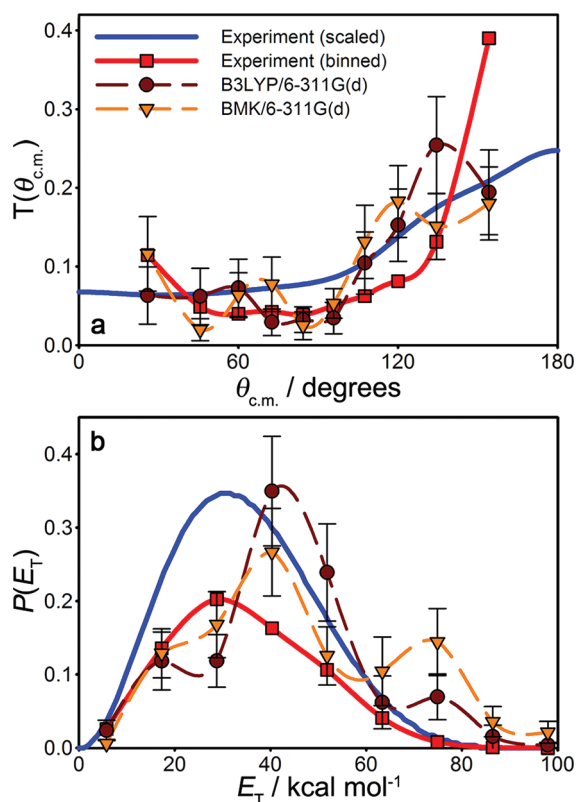


**Figure 12.** Comparison of laboratory and theoretical c.m. (a) angular and (b) translational energy distributions for the  $\text{O}(^3P) + \text{CO}_2$  isotope exchange reaction at  $\langle E_{\text{coll}} \rangle \approx 100 \text{ kcal mol}^{-1}$ . Distributions were binned using the bin midpoints shown here.

(31%).<sup>62</sup> The oxygen-atom abstraction yield is a lower bound because only a portion of the Newton sphere was observed (see Figure 4). Another uncertainty is in the assumption of mass-independent transmission of the quadrupole mass filter. Experience has shown that the lower mass-to-charge ratios have a lower

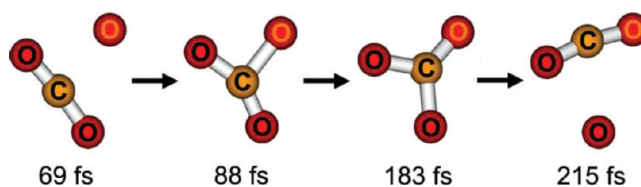


**Figure 13.** Snapshots of a QCT for  $\text{O}(^3P) + \text{CO}_2$  isotope exchange through a short-lived  $\text{CO}_3$  complex at  $34.6 \text{ kcal mol}^{-1}$  collision energy. The incident oxygen atom is highlighted for clarity.

transmission than higher mass-to-charge ratios. Thus, the relative yield of reactive products is probably overestimated, although we are not able to quantify the error.

Theoretical yields were estimated from the fraction of trajectories that led to reaction products. However, the current theoretical product yield for the isotope exchange reaction is an overestimate, because the range of impact parameters sampled was cutoff at  $5 a_0$ , below the collision diameter. As can be seen in the lower panel of Figure 8, the inelastic opacity function remained roughly constant over the entire range of impact parameters studied with no sign of falling off at  $5 a_0$ , indicating that only a subset of the nonreactive scattering was captured by the trajectories.

Experimental branching fractions for the isotope exchange reaction at  $\langle E_{\text{coll}} \rangle = 98.8 \text{ kcal mol}^{-1}$  and those calculated from the QCT calculations at  $E_{\text{coll}} = 103.8 \text{ kcal mol}^{-1}$  are shown in Table 4. The apparent agreement is fortuitous, as the range of impact parameters sampled in the theoretical results is truncated and both the theoretical and laboratory results have significant uncertainties; but the predicted and observed yields are certainly of the same order of magnitude, and they are both upper limits.

## V. DISCUSSION

**A. Dynamics of Nonreactive Scattering.** The agreement between experiment and calculations indicate that together our results provide a consistent description of the nonreactive (elastic and inelastic) scattering of O atoms and  $\text{CO}_2$ . The scattering is dominated by strong forward scattering of the  $\text{O}(^3P)$  atoms accompanied by minimal energy transfer. Large-impact-parameter collisions result in forward-scattered O atoms with little energy transferred (<10%) and a rapid decrease in scattered O-atom flux at larger angles. Scattering at the larger angles, which we observed experimentally as forward scattered  $^{12}\text{C}^{18}\text{O}_2$  products, required a second set of  $P(E_T)$  and  $T(\theta_{\text{c.m.}})$  distributions with significant energy transfer and essentially flat angular distribution in the sideways and forward directions. Thus, the product translational energy decreases as  $^{12}\text{C}^{18}\text{O}_2$  becomes more forward-scattered with respect to the direction of  $^{16}\text{O}$  (small  $\theta_{\text{c.m.}}$ , corresponding to low-impact-parameter collisions), that is, the  $^{12}\text{C}^{18}\text{O}_2$  are more internally excited in rebound collisions. Similar results have been observed in our studies of hyperthermal collisions of  $\text{O}(^3P)$  with  $\text{D}_2$ ,  $\text{CO}$ , and  $\text{C}_2\text{H}_6$ ,<sup>53–55</sup> of Ar with  $\text{C}_2\text{H}_6$  and, in the current results,  $\text{O}_2 + \text{CO}_2$ .

Hyperthermal inelastic scattering occurring via repulsive interactions has been studied in detail in a joint theoretical/experimental study on hyperthermal Ar +  $\text{C}_2\text{H}_6$ .<sup>63</sup> With ethane as the collision partner, there are a large number of internal degrees of freedom into which translational energy can be transferred upon collision. Calculated trajectories demonstrated the dependence of energy transfer on the impact parameter;

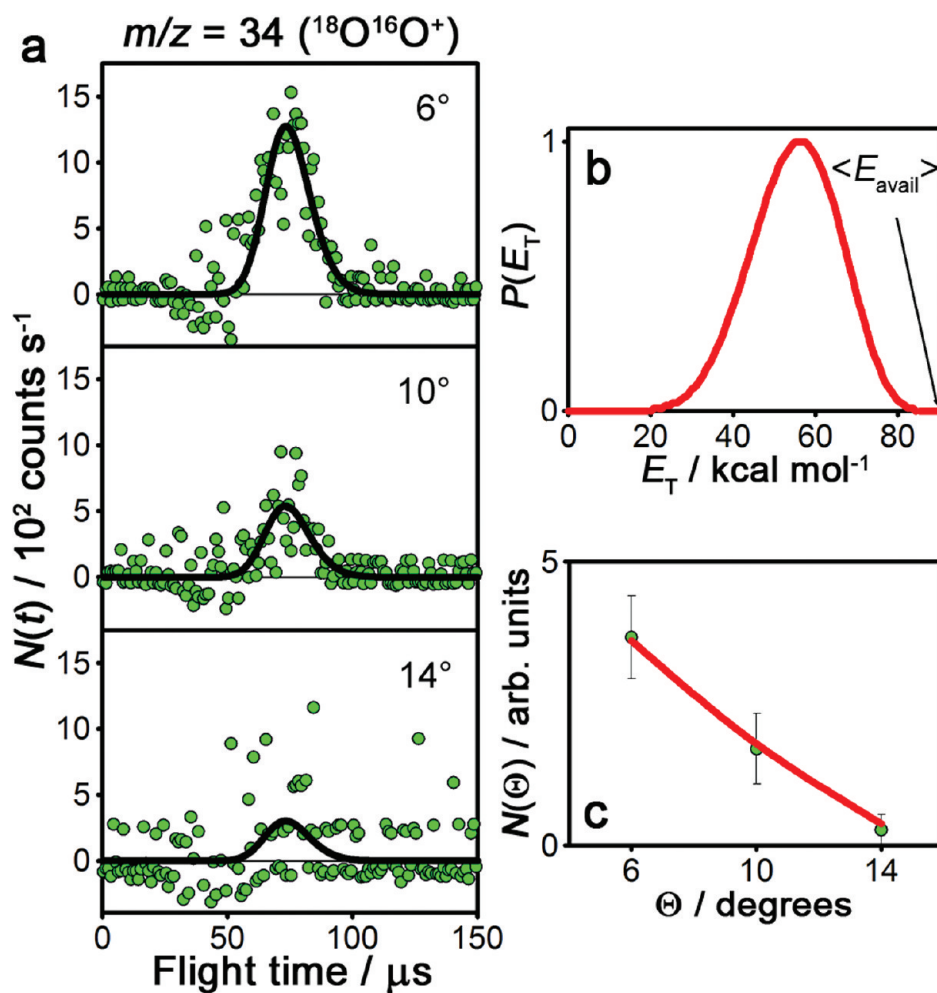


**Figure 14.** (a) Laboratory TOF, (b) c.m. translational energy, and (c) laboratory angular distributions for  $^{18}\text{O}^{16}\text{O}$  products of the  $^{16}\text{O}(^3P) + ^{12}\text{C}^{18}\text{O}_2 \rightarrow ^{18}\text{O}^{16}\text{O} + ^{12}\text{C}^{18}\text{O}$  reaction at  $\langle E_{\text{coll}} \rangle = 98.8 \text{ kcal mol}^{-1}$ . The circles in (a) and (c) are experimental data, while the lines are the best-fit forward-convolution simulations of the experimental data derived from the c.m. translational energy distribution shown in (b). The error bars in (c) represent  $2\sigma$  uncertainties in the integrated experimental TOF distributions (see Appendix A).

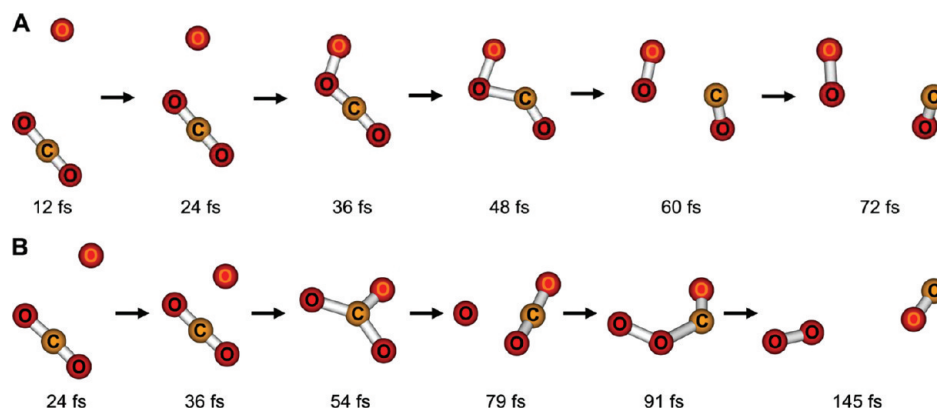


**Figure 15.** Snapshots of QCTs for the  $\text{O}(^3P) + \text{CO}_2 \rightarrow \text{O}_2 + \text{CO}$  reaction. (A) A stripping-type mechanism at  $149.8 \text{ kcal mol}^{-1}$  collision energy calculated at the B3LYP/6-311G(d) level of theory. (B) A  $\text{CO}_3$  reaction-complex mechanism at  $126.7 \text{ kcal mol}^{-1}$  collision energy calculated at the BMK/6-311G(d) level of theory. The incident oxygen atom is highlighted for clarity.

collisions at small impact parameters transfer more energy into vibration, reaching an asymptotic limit of approximately 20% energy transferred (86–91% at the peak of the

$P(E_T)$  distribution) for rebound collisions at energies of 2.6–5 eV, in good agreement with the experimentally observed distributions.

**Table 4. Comparison of Experimental and Theoretical Yields for the Products of  $O(^3P) + CO_2$  Collisions near  $100 \text{ kcal mol}^{-1}$ <sup>a</sup>**

	nonreactive scattering	oxygen isotope exchange
experiment	0.984(10)	0.016(10)
B3LYP/6-311G(d)	>0.982	<0.018
BMK/6-311G(d)	>0.981	<0.019

<sup>a</sup>Uncertainty in experimental yield is  $2\sigma$ .

The extent of energy transfer in rebound hyperthermal collisions (seen in forward scattering of the partner) varies considerably with system. The differences appear to reflect in part the available degrees of freedom. As described above, in Ar + ethane, the products from rebound collisions retained approximately 80% of the initial energy in translation. In hyperthermal  $O(^3P) + C_2H_6$  collisions, the forward scattered  $C_2H_6$   $P(E_T)$  peaks at approximately 60%, in good agreement with theory. In comparison, in hyperthermal collisions of  $O(^3P)$  with diatomic CO, 84% of the energy remained in product translation and was independent of angle; the data could be fit with a single set of  $P(E_T)$  and  $T(\theta_{c.m.})$  distributions. Energy transfer to a diatomic molecule such as CO has a low probability unless resonant.

We observed significant energy transfer in the  $O(^3P) + CO_2$  system, with an average of only 41% of the collision energy remaining in product translation. Such a large extent of energy transfer is at first glance surprising, given that  $CO_2$  has only three vibrational degrees of freedom. In contrast to the other systems, the  $O + CO_2$  system possesses a significant bound intermediate  $CO_3$ , and collisions at small impact parameters can sample the  $CO_3$  intermediate. Thus, we postulate that a second energy transfer mechanism, “failed” reactive trajectories, may be important. A  $^{16}O^{18}O_2^*$  complex can dissociate to yield products corresponding to either inelastic scattering or isotope exchange, depending on the identity of the departing atom. Large energy transfers would result from such failed reactive trajectories, if energy is significantly randomized during the lifetime of the complex. There is in fact a weak low energy tail in the  $P(E_T)$  distribution in  $^{16}O(^3P) + C^{18}O$  collisions (0.5% of the scattered  $C^{18}O$  have only <20% of the collision energy remaining in translation), which has similarly been attributed to failed reactive collisions.<sup>53</sup> Inelastic scattering via a complex mechanism is discussed in more detail below.

**B. Dynamics of Isotope Exchange and the  $CO_3$ -Complex Mechanism.** The theoretical results on  $^{16}O(^3P) + ^{12}C^{18}O_2 \rightarrow ^{18}O + ^{16}O^{12}C^{18}O$  collisions, though not entirely matching experimental results, provide a framework for interpreting the isotope exchange reaction as occurring via a relatively shallow  $CO_3$  intermediate. The ab initio calculations indicate that  $O(^3P)$  atoms colliding with  $CO_2$  at translational energies of  $E_T = 100 \text{ kcal mol}^{-1}$  have energies significantly above the barrier (24  $\text{kcal mol}^{-1}$ ) for formation of the triplet  $CO_3$  intermediate. The well of the  $CO_3$  intermediate is relatively shallow ( $\Delta E_{el} = 7.76 \text{ kcal mol}^{-1}$  at the W4 FCI limit). At these high energies, while many QCT trajectories become trapped in the  $CO_3$  complex, the well is sufficiently below the collision energy that some collisions are direct displacement reactions; these trajectories lead to the observed preference for backward scattering. In reactive trajectories that form a complex, the intermediate lives for up to several vibrational periods and is short-lived ( $\tau < 1 \text{ ps}$ ).

We find semiquantitative agreement between the experimental isotope-exchange results and the QCT-derived dynamics (see Figure 12). The angular distributions are in good agreement, but the calculations significantly overestimate the translational energy of the products. The  $P(E_T)$  distribution is predicted to peak rather sharply at  $\sim 40 \text{ kcal mol}^{-1}$ , whereas the experimentally observed distribution is slower and much broader ( $\langle E_T \rangle = 35 \text{ kcal mol}^{-1}$ ), peaking at  $30 \text{ kcal mol}^{-1}$ . There are several possible explanations. Experimentally, we detect  $^{16}O^{18}O$  products from collisions of both O and  $O_2$  with  $C^{18}O_2$  and have assigned the faster signal to scattering with  $O_2$ ; it is thus possible that some faster  $^{16}O^{18}O$  signal from  $O + CO_2$  was attributed to  $O_2 + CO_2$ . The QCT calculations are performed on B3LYP and BMK surfaces, which may not correctly describe the exit channel surface (B3LYP underestimates the barrier height by 6  $\text{kcal mol}^{-1}$ , though the BMK barrier agrees well with the W4 FCI limit). Errors in the surface may lead to errors in the coupling of translation and internal modes in the exit channel. Finally, both surfaces underestimate the depth of the  $CO_3$  well (by 2–3  $\text{kcal mol}^{-1}$  out of 7.8  $\text{kcal mol}^{-1}$ ), which will cause QCT calculations to underestimate the lifetime of the  $CO_3$  complex and the energy transfer to internal degrees of freedom.

The role of multiple potential energy surfaces may also be important. The QCT dynamics assume that the  $O(^3P) + CO_2$  isotope exchange reaction occurs entirely on the lowest triplet surface, of  $^3A''$  symmetry, whereas the reaction can sample three different triplet PESs (one of  $^3A'$  symmetry and two of  $^3A''$  symmetry in planar configurations). Critically, two surfaces (one  $^3A'$  and one  $^3A''$ ) are nearly degenerate in the region of  $CO_3$ , with the transition state for the  $^3A'$  surface only 2.69  $\text{kcal mol}^{-1}$  above that for the ground state. Collisions on both surfaces are thus likely to be important. Breaking of the plane of symmetry will lead to mixing of the states as the reactants approach each other, which should promote surface hopping.

Vibronic coupling could be especially significant in the  $CO_3$  intermediate. In EOM-EE(2,3) calculations, Kowalczyk and Krylov<sup>64</sup> have predicted that there are two low-lying triplet states of  $CO_3$  in  $D_{3h}$  symmetry,  $^3E'$  and  $^3E''$  states, with vertical excitation energies of approximately 1.1–1.2 eV above a computed singlet  $D_{3h}$  state. Both of these states must exhibit the Jahn–Teller effect. These predicted states (which are not geometrically optimized) lie fairly close to the  $^3A'$  and  $^3A''$  states that we find in this work. Those states are nearly degenerate at the  $CO_3$  minimum, split by only 0.07  $\text{kcal mol}^{-1}$  at the W4 full CI/all electron level (see last column, Table 1), presumably the bound Jahn–Teller components of the predicted  $^3E'$  and  $^3E''$  states. The likelihood of strong vibronic coupling effects raises some concerns about the validity of density functional treatment of the  $CO_3$  intermediate. Furthermore, from the existence or near existence of two seams of conical intersections in the center of the  $CO_3$  space, we conclude that there is likely to be extensive vibronic coupling among all of these states in the course of reactions proceeding through the  $CO_3$  intermediate. Even if these intersections eventually funnel the reactants back onto the lowest triplet state, they would increase the phase space sampled in the  $CO_3$  region, leading to longer lifetimes and more energy relaxation than predicted by our classical mechanics on a single surface.

Trajectories proceeding through the complex intermediate can lead to either isotope exchange or inelastic scattering. The identity of the dissociating oxygen atom determines the reaction’s classification: if the dissociating oxygen atom is one originally on  $CO_2$ , then the trajectory is reactive; if it is the incident oxygen

atom, then the trajectory is inelastic. The possibility of a common intermediate is most evident in the forward-scattered CO<sub>2</sub> products of the two channels. The angular (for angles <90°) and translational energy distributions for forward scattered CO<sub>2</sub> products from inelastic scattering (see Figure 6) are very similar to those from isotope exchange (Figure 12). These results would suggest that the large energy transfer seen in inelastic O(<sup>3</sup>P) + CO<sub>2</sub> rebound collisions is in fact due to collisions occurring via the CO<sub>3</sub> intermediate.

There are some differences in the dynamics of the forward-scattered CO<sub>2</sub> products of inelastic versus reactive scattering collisions. At larger angles (less rebound-like), the inelastic  $T(\theta_{\text{c.m.}})$  distribution starts to increase rapidly, most likely due to contributions from higher impact parameter collisions on the repulsive wall. In addition, the slow inelastic  $P(E_{\text{T}})$  distribution ( $\langle E_{\text{T}} \rangle = 41 \text{ kcal mol}^{-1}$ ) is shifted to higher energies relative to the isotope exchange  $P(E_{\text{T}})$  distribution ( $\langle E_{\text{T}} \rangle = 35 \text{ kcal mol}^{-1}$ ). This difference may have several possible sources, including (1) experimental uncertainty, since reactive signals in both channels are blended with the O<sub>2</sub> + CO<sub>2</sub> inelastic scattering signal, (2) contributions from direct rebound inelastic collisions that do not sample the well, and (3) differences in dynamics of <sup>16</sup>O versus <sup>18</sup>O dissociation from the complex (i.e., the complex retains memory of the initial collision).

The data are not consistent with a mechanism involving a long-lived intermediate. In this model, complexes with deep wells or which are formed at low collision energies can persist for times longer than a rotational period. In this case, the lifetime of the complex determines the c.m. angular and translational energy distributions of product CO<sub>2</sub>. Longer-lived CO<sub>3</sub> complexes should yield smaller average translational energies, because they will have more time to redistribute the initial translational energy to internal degrees of freedom. If the lifetime is longer than a rotational period, there should be no memory of the initial impact direction, resulting in a symmetric product angular distribution.

Our results, however, are more consistent with a single direct mechanism via a short-lived complex. We observe that one  $P(E_{\text{T}})$  distribution successfully fits the experimentally observed energy release at all c.m. angles. The QCT calculations indicate that the complex is formed but lives for at most a few vibrational periods. If the complex lifetime is short, the broad angular distribution would be caused by dynamical effects, rather than by rotational averaging of the dissociation vector over all complex orientations. Once over the barrier, formation of the CO<sub>3</sub> complex suggests that the identity of the O atoms becomes scrambled and that memory of which O atom is the incident one is lost (this does not require, however, that the energy be statistically randomized). The extent of isotopic scrambling could come from measuring the ratio of forward scattered CO<sub>2</sub> products in the inelastic channel versus isotope exchange.

Despite the short predicted lifetimes, experiment and theory indicate substantial energy randomization in the complex. The  $P(E_{\text{T}})$  distribution peaks at 35 kcal mol<sup>-1</sup>, only 9 kcal mol<sup>-1</sup> above the predicted height of the exit channel barrier. Because the exit channel potential surface is likely to be steep, we expect that much of the barrier potential energy will be released into product translational energy. The experimental results are thus consistent with substantial if not complete energy randomization within the CO<sub>3</sub> complex.

Intersystem crossing (ISC) to form O(<sup>1</sup>D) could also account for some or all of the observed isotope exchange products. O(<sup>3</sup>P)

+ CO<sub>2</sub> collisions on the lowest triplet surface could, in principle, cross to the <sup>1</sup>A' surface to yield reactively scattered O(<sup>1</sup>D) + CO<sub>2</sub> products ( $\Delta H = 46 \text{ kcal mol}^{-1}$ ). As can be seen in Figures 6b and 12b, most of the products are formed with enough internal energy to allow for the presence of excited O(<sup>1</sup>D) atoms. We evaluated the possibility of ISC in our experiments by performing forward-convolution fits of the laboratory data that included the 46 kcal mol<sup>-1</sup> endothermicity of O(<sup>1</sup>D) versus O(<sup>3</sup>P). Satisfactory fits of the laboratory TOF and angular distributions were obtained (see Figure S7); consequently, ISC cannot be ruled out by the experimental data. No evidence for ISC was observed during our previous dynamics studies performed at similar hyperthermal velocities;<sup>52,54</sup> however, the possibility of ISC depends on the location of the seam of surface intersection for any given system, because the probability decreases exponentially with increasing relative velocity.<sup>65,66</sup> In the case of O + CO<sub>2</sub>, Kowalczyk and Krylov<sup>64</sup> and Liu et al.<sup>67</sup> have found several low-lying singlet CO<sub>3</sub> states, in addition to the triplet states of CO<sub>3</sub> described above. Mebel et al. have found one intersection near the O(<sup>1</sup>D) + CO<sub>2</sub> entrance channel to form singlet CO<sub>3</sub>, and other singlet–triplet crossings in the vicinity of bound CO<sub>3</sub> are possible.<sup>6</sup> Favorable Franck–Condon factors could lead to relatively facile singlet–triplet conversion, while the system samples the CO<sub>3</sub> subspace.

This mechanism for the O(<sup>3</sup>P) + CO<sub>2</sub> isotope exchange reaction can be compared with that observed by Perri et al. in molecular beam experiments on the isotope exchange reaction of O(<sup>1</sup>D) + CO<sub>2</sub> at low collision energies,  $\langle E_{\text{coll}} \rangle = 4.2$  and 7.7 kcal mol<sup>-1</sup>.<sup>12,13</sup> These authors observed two channels for isotope exchange: exchange with and without spin-quenching, O(<sup>1</sup>D) + CO<sub>2</sub> → O(<sup>3</sup>P) + CO<sub>2</sub> and O(<sup>1</sup>D) + CO<sub>2</sub> → O(<sup>1</sup>D) + CO<sub>2</sub>. In those experiments, the reactively scattered CO<sub>2</sub> products had an isotropic (forward–backward symmetric) angular distribution; those results were evidence for a CO<sub>3</sub> intermediate complex that lasted for at least several rotational periods (>1 ps). The singlet CO<sub>3</sub> intermediate is predicted to be 48.8 kcal mol<sup>-1</sup> deep, with no barrier on the singlet surface.<sup>6</sup> Two channels were observed, with average translational energies of 3.1 and 27 kcal mol<sup>-1</sup>. The authors attributed the large energy release in the second, major channel to intersystem crossing to the lower triplet potential energy surface (the translational energy corresponds to ~50% of the available energy including the exothermicity to form O(<sup>3</sup>P)).

**C. Dynamics of Oxygen Abstraction.** Our laboratory observation of <sup>16</sup>O/<sup>18</sup>O products together with the handful of QCT trajectories provide evidence for the presence of a weak oxygen abstraction reaction channel (8). The results thus far, however, are too preliminary to shed much light on the dynamics. There are indications that spectator stripping might be important, but the weak signal limits our ability to detect all but the fastest products (in the LAB frame) in a very narrow angular range, biasing the results in favor of detecting backward-scattered products (which would be a signature of a stripping mechanism). The QCT calculations find “stripping-type” oxygen abstraction trajectories only at the highest energy studied,  $E_{\text{coll}} = 149 \text{ kcal mol}^{-1}$ , 70–80 kcal mol<sup>-1</sup> above the barrier. At much lower collision energies, stripping may not be relevant, as most of the kinetic energy will be required to overcome the barrier and thus only the lowest-impact-parameter collisions can lead to reaction, that is, little energy will be available to be tied up as angular momentum.

Oxygen abstraction must proceed through TS2 or TS3. Hammond's postulate states that, for endothermic reactions, the transition state should be late and product-like. The small

endoothermicity relative to the barrier height for oxygen-atom abstraction (see Table 1) suggests, however, that TS2 and TS3 should be more reactant-like. Indeed, the bond lengths of CO and O<sub>2</sub> are significantly longer in TS2 and TS3 than at equilibrium for the individual molecules, which are 1.14 and 1.21 Å, respectively, calculated at the CCSD(T)/aug-cc-pVTZ level of theory.

It seems plausible that reaction (8) may first proceed with O-atom attack on the carbon, which has a significantly lower barrier and allows the O atom to form an activated complex with the CO<sub>2</sub>. The preliminary QCT calculations indicate that O<sub>2</sub> is then formed as a departing oxygen atom attaches to another O atom. The CO<sub>3</sub>-complex mechanism requires that the initially dissociating oxygen atom recoils slowly, providing sufficient time for the nascent CO<sub>2</sub> to rotate before the receding oxygen atom moves too far away for any further O–O interaction to occur. This mechanism resembles the “roaming” mechanisms identified for formaldehyde<sup>68</sup> and acetaldehyde<sup>69</sup> photodissociation. In contrast, if the O-atom recoil is too fast and the atom leaving the complex is different from the one that initially approached the CO<sub>2</sub>, an isotope exchange reaction would take place. Finally, if the recoil is too fast and the oxygen atom that initially approached the CO<sub>2</sub> leaves the complex, the result is inelastic scattering. These intriguing preliminary findings need to be corroborated by a more statistically meaningful number of trajectories at the actual collision energy.

**D. Atmospheric Implications.** Our laboratory observation of O(<sup>3</sup>P) + CO<sub>2</sub> isotope exchange may be relevant for models of oxygen isotope cycling in the middle and upper atmosphere because the models do not currently include O(<sup>3</sup>P) + CO<sub>2</sub> reactions explicitly. Only the O(<sup>1</sup>D) + CO<sub>2</sub> isotope exchange reaction (reaction barrier ≤ 1 kcal mol<sup>-1</sup>) has been considered in models of oxygen-isotope cycling through CO<sub>2</sub>, and the constraints offered by oxygen triple-isotope analysis (i.e., the <sup>18</sup>O/<sup>16</sup>O and <sup>17</sup>O/<sup>16</sup>O ratios) have not been sufficient to rule out the presence of another important oxygen-cycling channel.<sup>17,70–73</sup> Recently, a study of stratospheric <sup>16</sup>O<sup>13</sup>C<sup>18</sup>O revealed that the isotopic budget of stratospheric CO<sub>2</sub> may be more complex than previously thought: the O(<sup>1</sup>D) + CO<sub>2</sub> reaction, while it could explain midlatitude variations in <sup>16</sup>O<sup>13</sup>C<sup>18</sup>O proportions, could not fully explain the proportions of <sup>16</sup>O<sup>13</sup>C<sup>18</sup>O observed in the polar vortex.<sup>16</sup> Effects due to subsidence of the mesosphere and heterogeneous chemistry in the polar vortex may be important.

Here, we suggest that O(<sup>3</sup>P) + CO<sub>2</sub> reactions in the upper atmosphere could significantly affect the oxygen isotope distribution in CO<sub>2</sub>. The O(<sup>3</sup>P) + CO<sub>2</sub> isotope exchange reaction could yield isotope effects qualitatively different from those in the O(<sup>1</sup>D) + CO<sub>2</sub> reaction because its mechanism is direct, unlike the mechanism involving a long-lived CO<sub>3</sub>\* intermediate for the O(<sup>1</sup>D) + CO<sub>2</sub> reaction.<sup>12,13</sup> Instead, like the O<sub>3</sub>\* complex in the O(<sup>3</sup>P) + O<sub>2</sub> isotope exchange reaction,<sup>74</sup> the CO<sub>3</sub>\* reaction complex formed from O(<sup>3</sup>P) + CO<sub>2</sub> is not sufficiently long-lived for its energy to randomize; thus, dynamical isotope effects are likely to be important to its isotope-specific branching fractions. These types of nonstatistical isotope effects are believed to play a role in determining “anomalous” formation rates of stable O<sub>3</sub> from the O<sub>3</sub>\* complex for different isotopologues.<sup>75–77</sup>

As a result of limitations in the range of collision energies available in our experiment, we were unable to investigate the O(<sup>3</sup>P) + CO<sub>2</sub> isotope exchange dynamics at or near the reaction threshold, which is the collision-energy regime most relevant to the atmosphere. Our calculated reactive trajectories at  $E_{\text{coll}} = 23.1$

and 34.6 kcal mol<sup>-1</sup> suggest, however, that isotope exchange is direct at collision energies just above the reaction barrier (see Figure 13).

Of course, one must be careful to distinguish between non-statistical energy randomization and nonstatistical isotope effects; for example, formation of CO<sub>3</sub> even within a vibrational period could lead to all three C–O bonds being equally likely to dissociate, even if the energy is not distributed according to RRKM theory. Thus, even a “direct” reaction could lead to a “statistical” distribution of isotopically substituted products.

The overall importance of O(<sup>3</sup>P) + CO<sub>2</sub> isotope exchange reactions to oxygen cycling in the atmosphere depends on both the excitation function of the reaction and the proportion of O(<sup>3</sup>P) in the atmosphere with sufficient translational energy to surmount the reaction barrier. The best W4 energy for TS1 (<sup>3</sup>A'', 24.08 kcal mol<sup>-1</sup>) implies that relative velocities of ≥ 3 km s<sup>-1</sup> are required to open the isotope exchange channel; ozone photolysis in the Hartley band (220–310 nm) and at shorter wavelengths yields O(<sup>3</sup>P) + O<sub>2</sub>(<sup>3</sup>Σ<sub>g</sub><sup>-</sup>) photofragments having a broad translational energy distribution, with a significant population having translational energies of 25–100 kcal mol<sup>-1</sup>.<sup>2,78–82</sup> Furthermore, the quantum yield of fast O(<sup>3</sup>P) appears to increase with decreasing wavelength, with a branching fraction of at least 17% at 193 nm.<sup>2,82</sup> Our hard-sphere collision modeling (see refs 78 and 79 for method details) using (1) an approximate O(<sup>3</sup>P) velocity distribution based on that reported by Stranges et al.<sup>2</sup> for O<sub>3</sub> photodissociation at 193 nm, and (2) cross sections for the electronic and velocity relaxation of oxygen atoms by N<sub>2</sub>,<sup>83,84</sup> suggests that the size of the reactive O(<sup>3</sup>P) reservoir could be as high as several percent that of O(<sup>1</sup>D). Future theoretical and experimental studies can elucidate the shape of the reaction's excitation function near the threshold and the O(<sup>3</sup>P) photofragment yield and velocity distribution across the actinic spectrum; these data are needed before an appropriate atmospheric simulation can be constructed. We note that a recent laboratory study of the O<sub>2</sub>/O<sub>3</sub>/CO<sub>2</sub> photochemical system showed deviations from modeled results at long irradiation times ( $t \sim$  days) when a mercury lamp was used as an actinic light source (185 and 254 nm emission lines);<sup>16</sup> a minor O(<sup>3</sup>P) + CO<sub>2</sub> isotope exchange channel could address part of this discrepancy as well as some of the disagreements between earlier studies of O<sub>2</sub>/O<sub>3</sub>/CO<sub>2</sub> photochemistry.<sup>10,11,14,15</sup> This hypothesis awaits further testing, however, perhaps with systematic studies of the O<sub>2</sub>/O<sub>3</sub>/CO<sub>2</sub> photochemical system as a function of actinic wavelength.

## VI. CONCLUSIONS

We have investigated the dynamics of O(<sup>3</sup>P) + CO<sub>2</sub> collisions at hyperthermal energies. Nonreactive scattering was dominated by high-impact-parameter collisions, which did not perturb the initial velocity of the reactants significantly. Lower impact parameters resulted in increased translational-to-internal energy transfer. Both oxygen isotope exchange and atom abstraction reaction channels were observed. The oxygen isotope exchange reaction displayed an angular distribution that is peaked in the backward direction with a large amount of translational-to-internal energy transfer, suggesting that the reaction occurs at low impact parameters through a short-lived intermediate CO<sub>3</sub>\* complex. This mechanism was supported by QCT calculations; relative product yields and reaction cross sections that were in agreement with experiment were obtained. The QCT calculations also suggested that O-atom abstraction reactions occur

either through a stripping mechanism or by way of a  $\text{CO}_3^*$  complex, although the experimental data were insufficient to suggest either pathway. The isotope exchange reaction may be important for the oxygen isotope budget of the middle and upper atmosphere because hyperthermal  $\text{O}(^3\text{P})$  is a product of  $\text{O}_3$  photolysis.

This work has further implications for previous computational studies of hyperthermal  $\text{O}(^3\text{P}) + \text{CO}_2$  scattering dynamics, as previous PESs did not include the isotope exchange channel when calculating cross sections for vibrational (stretch and/or bend) excitation. Those studies, consequently, likely underestimated the cross sections for vibrational excitation. Furthermore, the total vibrationally inelastic cross sections previously calculated are comparable to the reaction cross sections calculated in this study. Explicit inclusion of this region of the  $\text{CO}_3$  PES is necessary, particularly in light of our observations of “failed” isotope exchange QCTs (inelastic products formed via the  $\text{CO}_3$  intermediate). These trajectories will impact the calculated state-specific cross sections of  $\text{O}(^3\text{P})-\text{CO}_2$  energy transfer.

Lastly, nonadiabaticity during inelastic and reactive trajectories cannot be ruled out and its effects should be investigated. Both inelastic and reactive trajectories may be sensitive to the coupling between the lowest triplet ( $^3\text{A}''$ ) PES and nearby electronic surfaces. Moreover, the  $\text{O}(^3\text{P})$  atom is equally likely to approach the  $\text{CO}_2$  on any of three surfaces (two  $^3\text{A}''$  and one  $^3\text{A}'$ ), as these surfaces are degenerate at large  $\text{O}-\text{CO}_2$  separations. In particular, there appears to be a second triplet potential energy surface forming a  $\text{CO}_3$  complex with barrier and intermediate  $\text{CO}_3$  energies close to those of the lowest surface. The existence of or near existence of two seams of conical intersection at the  $\text{CO}_3$  intermediate indicates strong coupling during the course of reaction. With  $\sim 100 \text{ kcal mol}^{-1}$  collision energy, the experiment may probe regions of the PES far from the TS1, TS2, TS3, and  $\text{CO}_3$  structures; the presence of several other surfaces (both triplet and singlet) within this energy range, the possibility of vibronic effects due to Jahn–Teller-like distortion, and the inability of density-functional methods to capture the dynamics quantitatively all suggest that a higher level treatment of the PES may be necessary.

## APPENDIX A: ESTIMATING THE UNCERTAINTY IN THE LABORATORY-FRAME ANGULAR DISTRIBUTIONS

For this analysis, we treat the TOF distribution at a given laboratory angle,  $\Theta$ , as a type of Monte Carlo integration of the “true” TOF distribution, and we estimate the variance in the integrated area accordingly. Under this approximation, the integrated area,  $I(\Theta)$ , is equivalent to the area of a rectangle with a width equal to the total time range,  $t_{\text{total}}$ , and height equal to the average number density over that time range,  $\langle N(t) \rangle_{\text{total}}$ . More formally, this relation can be written as a discrete sum over the channels on the MCS, each of which corresponded to a  $1 \mu\text{s}$  dwell time:

$$I(\Theta) = \sum_{i=1}^{t_{\text{total}}} N(t_i) = t_{\text{total}} \left[ \frac{1}{t_{\text{total}}} \sum_{i=1}^{t_{\text{total}}} N(t_i) \right] = t_{\text{total}} \langle N(t) \rangle_{\text{total}}$$

The variance of  $I(\Theta)$  must be evaluated as a function of time because the number density at a given arrival time at the detector,  $N(t)$ , varied with flight time in each TOF distribution. Consequently, the TOF distribution was further divided into a set of bins for which the variance was calculated and summed over the

total TOF distribution using the following relations:

$$\sigma_{N(t)_{\text{bin}}}^2 = \frac{1}{t_{\text{bin}}} \sum_i^f [t_{\text{bin}} N(t_i)]^2 - [t_{\text{bin}} \langle N(t) \rangle_{\text{bin}}]^2$$

and

$$\sigma_{I(\Theta)}^2 = \sum_{\text{bins}} \sigma_{N(t)_{\text{bin}}}^2$$

where  $i$  and  $f$  represent the first and last members of each data bin. The standard deviation,  $\sigma_{I(\Theta)}$ , was calculated by taking the square root of the variance. We note some degree of sensitivity in the calculated  $\sigma_{I(\Theta)}$  values on  $t_{\text{bin}}$  because the  $N(t)$  distributions show significant structure. Consequently, we have reported conservative estimates of  $\sigma_{I(\Theta)}$  using the minimum bin size of  $t_{\text{bin}} = 3 \mu\text{s}$ , or 3 data points per  $\sigma N(t)_{\text{bin}}$  calculation.

## ASSOCIATED CONTENT

**S Supporting Information.** W4 benchmarking calculations on the  $\text{O}(^3\text{P}) + \text{HCl}$  system. Details of the experimental parameters. The laboratory-to-c.m. frame coordinate transformation. Theoretical translational energy and angular distributions for the isotope exchange reaction. Representative TOF distributions for nonreactive  $\text{O}_2 + \text{CO}_2$  collisions, their best-fit forward-convolution simulations, and their  $P(E_T)$ ,  $T(\theta_{\text{c.m.}})$ , and  $T(\Theta_{\text{lab}})$  distributions. Animations of representative  $\text{O}(^3\text{P}) + \text{CO}_2$  trajectories: (1) oxygen isotope exchange through a short-lived  $\text{CO}_3$  intermediate, (2) oxygen isotope exchange through a longer-lived  $\text{CO}_3$  intermediate, (3) oxygen-atom abstraction through a  $\text{CO}_3^*$ -complex mechanism that would result in  $^{18}\text{O}_2$  products experimentally, and (4) oxygen-atom abstraction through a  $\text{CO}_3^*$ -complex mechanism that would result in  $^{18}\text{O}^{16}\text{O}$  products experimentally. This material is available free of charge via the Internet at <http://pubs.acs.org>.

## AUTHOR INFORMATION

### Corresponding Author

\*E-mail: [mo@its.caltech.edu](mailto:mo@its.caltech.edu); [tminton@montana.edu](mailto:tminton@montana.edu); [schatz@chem.northwestern.edu](mailto:schatz@chem.northwestern.edu).

### Present Addresses

<sup>†</sup>Department of Earth and Space Sciences, University of California, Los Angeles, CA, 90095, U.S.A.

<sup>‡</sup>Department of Chemistry, University of Tennessee, Knoxville, TN 37996, U.S.A.

## ACKNOWLEDGMENT

We thank Ned F. Lindholm for experimental assistance. This work was supported in part by the Missile Defense Agency under cooperative agreement HQ0006-05-2-0001. L.Y.Y. was supported by the Davidow Fund (Caltech), and G.C.S. was supported by the Air Force Office of Scientific Research grant FA955D-10-1-0205. Research at Weizmann Institute was partially supported by the Helen and Martin Kimmel Center for Molecular Design and by the Israel Science Foundation. J.M.L.M. is the incumbent of the Baroness Thatcher Professorial Chair of Chemistry.

## REFERENCES

- (1) Matsumi, Y.; Kawasaki, M. *Chem. Rev.* **2003**, *103*, 4767.
- (2) Stranges, D.; Yang, X.; Chesko, J. D.; Suits, A. G. *J. Chem. Phys.* **1995**, *102*, 6067.

- (3) Sharma, R. D.; Roble, R. G. *ChemPhysChem* **2002**, *3*, 841.
- (4) Averyanov, A. S.; Khait, Y. G.; Puzanov, Y. V. *J. Mol. Struct.: THEOCHEM* **1999**, *459*, 95.
- (5) Froese, R. D. J.; Goddard, J. D. *J. Phys. Chem.* **1993**, *97*, 7484.
- (6) Mebel, A. M.; Hayashi, M.; Kislov, V. V.; Lin, S. H. *J. Phys. Chem. A* **2004**, *108*, 7983.
- (7) Bennett, C. J.; Jamieson, C.; Mebel, A. M.; Kaiser, R. I. *Phys. Chem. Chem. Phys.* **2004**, *6*, 735.
- (8) Baulch, D. L.; Breckenridge, W. H. *Trans. Faraday Soc.* **1966**, *62*, 2768.
- (9) DeMore, W. B.; Dede, C. *J. Phys. Chem.* **1970**, *74*, 2621.
- (10) Chakraborty, S.; Bhattacharya, S. K. *J. Geophys. Res.* **2003**, *108*, 4724.
- (11) Johnston, J. C.; Röckmann, T.; Brenninkmeijer, C. A. M. *J. Geophys. Res.* **2000**, *105*, 15.
- (12) Perri, M. J.; Van Wyngarden, A. L.; Boering, K. A.; Lin, J. J.; Lee, Y. T. *J. Chem. Phys.* **2003**, *119*, 8213.
- (13) Perri, M. J.; Van Wyngarden, A. L.; Lin, J. J.; Lee, Y. T.; Boering, K. A. *J. Phys. Chem. A* **2004**, *108*, 7995.
- (14) Shaheen, R.; Janssen, C.; Röckmann, T. *Atmos. Chem. Phys.* **2007**, *7*, 495.
- (15) Wen, J.; Thiemens, M. H. *J. Geophys. Res.* **1993**, *98*, 12.
- (16) Yeung, L. Y.; Affek, H. P.; Hoag, K. J.; Guo, W.; Wiegel, A. A.; Atlas, E. L.; Schauflyer, S. M.; Okumura, M.; Boering, K. A.; Eiler, J. M. *Proc. Natl. Acad. Sci. U.S.A.* **2009**, *106*, 11496.
- (17) Thiemens, M. H.; Jackson, T.; Zipf, E. C.; Erdman, P. W.; van Egmond, C. *Science* **1995**, *270*, 969.
- (18) Boering, K. A.; Jackson, T.; Hoag, K. J.; Cole, A. S.; Perri, M. J.; Thiemens, M.; Atlas, E. *Geophys. Res. Lett.* **2004**, *31*, L03109.
- (19) Hoag, K. J.; Still, C. J.; Fung, I. Y.; Boering, K. A. *Geophys. Res. Lett.* **2005**, *32*, L02802.
- (20) Bass, J. N. *J. Chem. Phys.* **1974**, *60*, 2913.
- (21) Garrett, B. C. *Chem. Phys.* **1983**, *87*, 63.
- (22) Harvey, N. M. *Chem. Phys. Lett.* **1982**, *88*, 553.
- (23) Schatz, G. C.; Redmon, M. J. *Chem. Phys.* **1981**, *58*, 195.
- (24) Billing, G. D.; Clary, D. C. *Chem. Phys.* **1983**, *80*, 213.
- (25) de Lara-Castells, M. P.; Hernández, M. I.; Delgado-Barrio, G.; Villarreal, P.; López-Puertas, L. *J. Chem. Phys.* **2006**, *124*, 164302.
- (26) de Lara-Castells, M. P.; Hernández, M. I.; Delgado-Barrio, G.; Villarreal, P.; López-Puertas, L. *Mol. Phys.* **2007**, *105*, 1171.
- (27) Tsang, W.; Hampson, R. F. *J. Phys. Chem. Ref. Data* **1986**, *15*, 1087.
- (28) Oakes, D. B.; Sonnenfroh, D. M.; Caledonia, G. E.; Blumberg, W. A. M. *J. Geophys. Res.* **1994**, *99*, 23249.
- (29) Upschulte, B. L.; Caledonia, G. E. *J. Chem. Phys.* **1992**, *96*, 2025.
- (30) Castle, K. J.; Kleissas, K. M.; Rhinehard, J. M.; Hwang, E. S.; Dodd, J. A. *J. Geophys. Res.* **2006**, *111*, A09303.
- (31) Scott, G. B. I.; Pollock, D. S.; Phillips, L. F. *J. Chem. Soc., Faraday Trans.* **1993**, *89*, 1183.
- (32) Becke, A. D. *J. Chem. Phys.* **1993**, *98*, 5648.
- (33) Lee, C.; Yang, W.; Parr, R. G. *Phys. Rev. B* **1988**, *37*, 785.
- (34) Frisch, M. J.; Pople, J. A.; Binkley, J. S. *J. Chem. Phys.* **1984**, *80*, 3265.
- (35) Boese, A. D.; Martin, J. M. L. *J. Chem. Phys.* **2004**, *121*, 3405.
- (36) Raghavachari, K.; Trucks, G. W.; Head-Gordon, M.; Pople, J. A. *Chem. Phys. Lett.* **1989**, *157*, 479.
- (37) Kendall, R. A.; Dunning, T. J.; Harrison, R. J. *J. Chem. Phys.* **1992**, *96*, 6796.
- (38) Shao, Y.; Molnar, L. F.; Jung, Y.; Kussmann, J.; Ochsenfeld, C.; Brown, S. T.; Gilbert, A. T. B.; Slipchenko, L. V.; Levchenko, S. V.; O'Neill, D. P.; DiStasio, R. A.; Lochan, R. C.; Wang, T.; Beran, G. J. O.; Besley, N. A.; Herbert, J. M.; Lin, C. Y.; Van Voorhis, T.; Chien, S. H.; Sodt, A.; Steele, R. P.; Rassolov, V. A.; Maslen, P. E.; Korambath, P. P.; Adamson, R. D.; Austin, B.; Baker, J.; Byrd, E. F. C.; Dachsel, H.; Doerksen, R. J.; Dreuw, A.; Dunietz, B. D.; Dutoi, A. D.; Furlani, T. R.; Gwaltney, S. R.; Heyden, A.; Hirata, S.; Hsu, C. P.; Kedziora, G.; Khalliulin, R. Z.; Klunzinger, P.; Lee, A. M.; Lee, M. S.; Liang, W.; Lotan, I.; Nair, N.; Peters, B.; Proynov, E. I.; Pieniazek, P. A.; Rhee, Y. M.; Ritchie, J.; Rosta, E.; Sherrill, C. D.; Simmonett, A. C.; Subotnik, J. E.; Woodcock, H. L.; Zhang, W.; Bell, A. T.; Chakraborty, A. K.; Chipman, D. M.; Keil, F. J.; Warshel, A.; Hehre, W. J.; Schaefer, H. F.; Kong, J.; Krylov, A. I.; Gill, P. M. W.; Head-Gordon, M. *Phys. Chem. Chem. Phys.* **2006**, *8*, 3172.
- (39) Werner, H.-J.; Knowles, P. J.; Lindh, R.; Manby, F. R.; Schutz, M.; Celani, P.; Korona, T.; Rauhut, G.; Amos, R. D.; Bernhardsson, A.; Berning, A.; Cooper, D. L.; Deegan, M. J. O.; Dobbyn, A. J.; Eckert, F.; Hampel, C.; Hetzer, G.; Lloyd, A. W.; McNicholas, S. J.; Meyer, W.; Mura, M. E.; Nicklass, A.; Palmieri, P.; Pitzer, R.; Schumann, U.; Stoll, H.; Stone, A. J.; Tarroni, R.; Thorsteinsson, T. *MOLPRO*, a package of ab initio programs, 2006.1, see www.molpro.net.
- (40) Karton, A.; Rabinovich, E.; Martin, J. M. L.; Ruscic, B. *J. Chem. Phys.* **2006**, *125*, 144108.
- (41) Ruscic, B.; Pinzon, R. E.; Morton, M. L.; von Laszewski, G.; Bittner, S. J.; Nijssure, S. G.; Amin, K. A.; Minkoff, M.; Wagner, A. F. *J. Phys. Chem. A* **2004**, *108*, 9979.
- (42) Karton, A.; Martin, J. M. L.; Taylor, P. R. *J. Chem. Phys.* **2007**, *127*, 064104.
- (43) Karton, A.; Daon, S.; Martin, J. M. L. *Chem. Phys. Lett.* **2011**, *510*, 165.
- (44) Lee, T. J.; Taylor, P. R. *Int. J. Quantum Chem., Quantum Chem. Symp.* **1989**, *23*, 199; Lee, T. J.; Rice, J. E.; Scuseria, G. E.; Schaefer, H. F., III *Theor. Chim. Acta* **1989**, *75*, 81.
- (45) Lee, T. J. *Chem. Phys. Lett.* **2003**, *372*, 362. Leininger, M. L.; Nielsen, I. M. B.; Crawford, T. D.; Janssen, C. L. *Chem. Phys. Lett.* **2000**, *328*, 431. Janssen, C. L.; Nielsen, I. M. B. *Chem. Phys. Lett.* **1998**, *290*, 423. Nielsen, I. M. B.; Janssen, C. L. *Chem. Phys. Lett.* **1999**, *310*, 568.
- (46) Bunker, D. L. In *Proceedings of the International School of Physics Enrico Fermi Course XLIV: Molecular Beam and Reaction Kinetics*; Schlier, C., Ed.; Academic Press: New York, 1970; p 315.
- (47) Press, W. H.; Flannery, B. P.; Teukolsky, S. A.; Vetterling, W. T. *Numerical Recipes in FORTRAN: The Art of Scientific Computing*, 2nd ed.; Cambridge University Press: Cambridge, U.K., 1992.
- (48) Levine, R. D. *Molecular Reaction Dynamics*; Cambridge University Press: Cambridge, U.K., 2005.
- (49) Hirschfelder, J. O.; Curtiss, C. F.; Bird, R. B. *Molecular Theory of Gases and Liquids*; John Wiley & Sons, Inc.: New York, 1964.
- (50) Némethy, G.; Pottle, M. S.; Scheraga, H. A. *J. Phys. Chem.* **1983**, *87*, 1883.
- (51) Hirschfelder, J. O.; Meath, W. J. The Nature of Intermolecular Forces. In *Adv. Chem. Phys.*; Hirschfelder, J. O., Ed.; Interscience Publishers: New York, 1967; Vol. 12.
- (52) Brunsvold, A. L.; Zhang, J.; Upadhyaya, H. P.; Minton, T. K.; Camden, J. P.; Paci, J. T.; Schatz, G. C. *J. Phys. Chem. A* **2007**, *111*, 10907.
- (53) Brunsvold, A. L.; Upadhyaya, H. P.; Zhang, J.; Cooper, R.; Minton, T. K.; Braunstein, M.; Duff, J. W. *J. Phys. Chem. A* **2008**, *112*, 2192.
- (54) Garton, D. J.; Brunsvold, A. L.; Minton, T. K.; Troya, D.; Maiti, B.; Schatz, G. C. *J. Phys. Chem. A* **2006**, *110*, 1327.
- (55) Garton, D. J.; Minton, T. K.; Hu, W.; Schatz, G. C. *J. Phys. Chem. A* **2009**, *113*, 4722.
- (56) Brink, G. O. *Rev. Sci. Instrum.* **1966**, *37*, 857.
- (57) Daly, N. R. *Rev. Sci. Instrum.* **1960**, *31*, 264.
- (58) Lee, Y. T. Reactive Scattering I: Nonoptical Methods. In *Atomic and Molecular Beam Methods*; Scoles, G., Ed.; Oxford University Press: New York, 1988; Vol. 1; p 533.
- (59) Yeung, L. Y.; Okumura, M.; Paci, J. T.; Schatz, G. C.; Zhang, J.; Minton, T. K. *J. Am. Chem. Soc.* **2009**, *131*, 13940.
- (60) The c.m. angular distribution for scattered  $^{16}\text{O}$  at  $\theta_{\text{c.m.}} \sim 0^\circ$  is an extrapolation because of high background from the hyperthermal oxygen source at the small laboratory angles corresponding to small c.m. angles for  $^{16}\text{O}$ . Most of the  $^{16}\text{O}$  probably scatters forward through high-impact-parameter collisions, but the limited constraints on the  $\theta_{\text{c.m.}} \sim 0^\circ$  angular distribution (e.g., the laboratory-frame angular distribution, which only probes  $\Theta \geq 6^\circ$ ) increase the uncertainty in that part of the c.m. angular distribution. This extrapolation had an effect on the relative product yield measurements but did not alter the results qualitatively.

- (61) Blank, D. A.; Hemmi, N.; Suits, A. G.; Lee, Y. T. *Chem. Phys.* **1998**, *231*, 261.
- (62) Our sensitivity study on the  $\theta_{\text{c.m.}} \rightarrow 0^\circ$  extrapolation we used for scattered  $^{16}\text{O}$  in the laboratory nonreactive scattered channel resulted in the nonreactive scattering and oxygen isotope-exchange branching fractions varying by  $\sim 0.005$  (approximately 20% relative error) when the scattered intensity at  $\theta_{\text{c.m.}} < 4^\circ$  was changed from twice the best-fit value to zero.
- (63) Brunsvold, A. L.; Garton, D. J.; Minton, T. K.; Troya, D.; Schatz, G. C. *J. Chem. Phys.* **2004**, *121*, 11702.
- (64) Kowalczyk, T.; Krylov, A. I. *J. Phys. Chem. A* **2007**, *111*, 8271.
- (65) Landau, L. *Phys. Z. Sowjetunion* **1932**, *2*, 46.
- (66) Zener, C. *Proc. R. Soc. A* **1932**, *137*, 696.
- (67) Liu, Y.; Bersuker, I. B.; Zou, W.; Boggs, J. E. *J. Chem. Theory Comput.* **2009**, *5*, 2679.
- (68) Townsend, D.; Lahankar, S. A.; Lee, S. K.; Chambreau, S. D.; Suits, A. G.; Zhang, X.; Rheinecker, J.; Harding, L. B.; Bowman, J. M. *Science* **2004**, *306*, 1158.
- (69) Houston, P. L.; Kable, S. H. *Proc. Natl. Acad. Sci. U.S.A.* **2006**, *103*, 16079.
- (70) Liang, M.-C.; Blake, G. A.; Lewis, B. R.; Yung, Y. L. *Proc. Natl. Acad. Sci. U.S.A.* **2007**, *104*, 21.
- (71) Liang, M. C.; Blake, G. A.; Yung, Y. L. *J. Geophys. Res.* **2008**, *113*, D12305.
- (72) Yung, Y. L.; DeMore, W. B.; Pinto, J. P. *Geophys. Res. Lett.* **1991**, *18*, 13.
- (73) Yung, Y. L.; Lee, A. Y. T.; Irion, F. W.; DeMore, W. B.; Wen, J. *J. Geophys. Res.* **1997**, *102*, 10857.
- (74) Van Wyngarden, A. L.; Mar, K. A.; Boering, K. A.; Lin, J. J.; Lee, Y. T.; Lin, S.-Y.; Guo, H.; Lendvay, G. *J. Am. Chem. Soc.* **2007**, *129*, 2866.
- (75) Gao, Y. Q.; Marcus, R. A. *Science* **2001**, *293*, 259.
- (76) Babikov, D.; Kendrick, B. K.; Walker, R. B.; Pack, R. T. *J. Chem. Phys.* **2003**, *119*, 2577.
- (77) Schinke, R.; Grebenshchikov, S. Y.; Ivanov, M. V.; Fleurat-Lessard, P. *Annu. Rev. Phys. Chem.* **2006**, *57*, 625.
- (78) Fairchild, C. E.; Stone, E. J.; Lawrence, G. M. *J. Chem. Phys.* **1978**, *69*, 3632.
- (79) Kinugawa, T.; Sato, T.; Arikawa, T.; Matsumi, Y.; Kawasaki, M. *J. Chem. Phys.* **1990**, *93*, 3289.
- (80) Shamsuddin, S. M.; Inagaki, Y.; Matsumi, Y.; Kawasaki, M. *Can. J. Chem.* **1994**, *72*, 637.
- (81) Syage, J. A. *J. Phys. Chem.* **1995**, *99*, 16530.
- (82) Takahashi, K.; Taniguchi, N.; Matsumi, Y.; Kawasaki, M. *Chem. Phys.* **1998**, *231*, 171.
- (83) Matsumi, Y.; Shamsuddin, S. M.; Sato, Y.; Kawasaki, M. *J. Chem. Phys.* **1994**, *101*, 9610.
- (84) Matsumi, Y.; Chowdhury, A. M. S. *J. Chem. Phys.* **1996**, *104*, 7036.